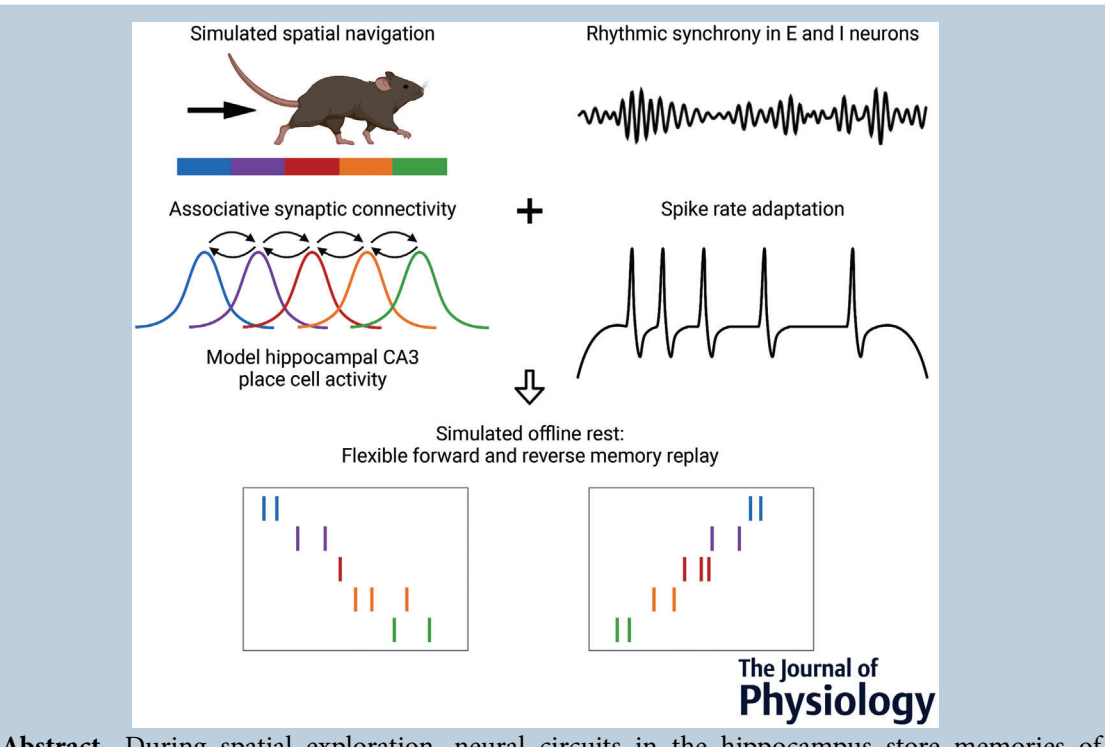
Check for updates

# Offline memory replay in recurrent neuronal networks emerges from constraints on online dynamics

Aaron D. Milstein<sup>1,2</sup> D, Sarah Tran<sup>1</sup>, Grace Ng<sup>1</sup> D and Ivan Soltesz<sup>1</sup>

Handling Editors: Katalin Toth & Jean-Claude Béïque

The peer review history is available in the Supporting information section of this article (https://doi.org/10.1113/JP283216#support-information-section).



**Abstract** During spatial exploration, neural circuits in the hippocampus store memories of sequences of sensory events encountered in the environment. When sensory information is absent during 'offline' resting periods, brief neuronal population bursts can 'replay' sequences of activity

Aaron Milstein is an Assistant Professor in the Department of Neuroscience and Cell Biology at Rutgers University. As a graduate student with Roger Nicoll, he integrated molecular biology, electrophysiology, and mathematical modelling to study synaptic transmission in the hippocampus. During a postdoc with Jeff Magee and Sandro Romani, he performed intracellular recordings from neuronal dendrites and built computational models to understand the role of dendritic calcium spikes in the formation of hippocampal place fields via behavioural timescale synaptic plasticity. As an instructor mentored by Ivan Soltesz, he developed biologically detailed neuronal network models to dissect the circuit components of memory.



S. Tran and G. Ng contributed equally to this study.

This article was first published as a preprint. Milstein AD, Tran S, Ng G, Soltesz I. 2022. Offline memory replay in recurrent neuronal networks emerges from constraints on online dynamics. bioRxiv. https://doi.org/10.1101/2021.10.27.466186.

<sup>&</sup>lt;sup>1</sup>Department of Neurosurgery, Stanford University School of Medicine, Stanford, CA, USA

<sup>&</sup>lt;sup>2</sup>Department of Neuroscience and Cell Biology, Robert Wood Johnson Medical School and Center for Advanced Biotechnology and Medicine, Rutgers University, Piscataway, NJ, USA

that resemble bouts of sensory experience. These sequences can occur in either forward or reverse order, and can even include spatial trajectories that have not been experienced, but are consistent with the topology of the environment. The neural circuit mechanisms underlying this variable and flexible sequence generation are unknown. Here we demonstrate in a recurrent spiking network model of hippocampal area CA3 that experimental constraints on network dynamics such as population sparsity, stimulus selectivity, rhythmicity and spike rate adaptation, as well as associative synaptic connectivity, enable additional emergent properties, including variable offline memory replay. In an online stimulus-driven state, we observed the emergence of neuronal sequences that swept from representations of past to future stimuli on the timescale of the theta rhythm. In an offline state driven only by noise, the network generated both forward and reverse neuronal sequences, and recapitulated the experimental observation that offline memory replay events tend to include salient locations like the site of a reward. These results demonstrate that biological constraints on the dynamics of recurrent neural circuits are sufficient to enable memories of sensory events stored in the strengths of synaptic connections to be flexibly read out during rest and sleep, which is thought to be important for memory consolidation and planning of future behaviour.

(Received 13 April 2022; accepted after revision 22 July 2022; first published online 30 July 2022) **Corresponding author** A. D. Milstein: 679 Hoes Lane West, Room 238, Piscataway, NJ 08854, USA. Email: milstein@cabm.rutgers.edu

Abstract figure legend During simulated rodent spatial navigation, place cells in hippocampal area CA3 fire at specific locations in space, generating a sequence in the order that the animal traverses. Recurrent network models of excitatory (E) place cells and inhibitory (I) interneurons that included associative synaptic connectivity between E cells, rhythmic synchrony in E and I cells, and spike rate adaptation in E cells were found to generate sequences in an offline state in the absence of structured sensory inputs. These sequences replayed those generated during navigation, but occurred in either forward or reverse order.

# **Key points**

- A recurrent spiking network model of hippocampal area CA3 was optimized to recapitulate experimentally observed network dynamics during simulated spatial exploration.
- During simulated offline rest, the network exhibited the emergent property of generating flexible forward, reverse and mixed direction memory replay events.
- Network perturbations and analysis of model diversity and degeneracy identified associative synaptic connectivity and key features of network dynamics as important for offline sequence generation.
- Network simulations demonstrate that population over-representation of salient positions like the site of reward results in biased memory replay.

# Introduction

In mammals, the hippocampus is a brain region involved in the storage and recall of spatial and episodic memories. As an animal explores a spatial environment, different subpopulations of hippocampal neurons known as 'place cells' are selectively activated at different positions in space, resulting in sequences of neuronal spiking that are on the seconds-long timescale of locomotor behaviour (O'Keefe & Conway, 1978). The synchronous firing of these sparse neuronal ensembles is coordinated by population-wide oscillations referred to as theta

( $\sim$ 4–10 Hz) and gamma ( $\sim$ 30–100 Hz) rhythms (Colgin, 2016). Within each cycle of the theta rhythm ( $\sim$ 125 ms), the spiking of active neurons is organized into fast timescale sequences such that neurons selective for just-visited positions spike first, then neurons selective for the current position, and finally neurons selective for the next and future positions spike last in the sequence (Drieu & Zugaro, 2019; Foster & Wilson, 2007). These order-preserving fast timescale 'theta sequences' are thought to be involved in planning and learning of event order through associative synaptic plasticity (Jensen et al., 1996; Kay et al., 2020).

4697793, 2023, 15, Downloaded from https://physoc.onlinelibrary.wiley.com/doi/10.1113/P283216, Wiley. Online Library on [29/02/2024]. See the Terms and Conditions (https://onlinelibrary.wiley.com/terms-and-conditions) on Wiley Online Library for rules of use; OA articles are governed by the applicable Certain Commons License

When an animal stop running, theta and gamma oscillations decrease, and neuronal circuits in the hippocampus instead emit intermittent synchronous bursts of activity that are associated with high-frequency oscillatory activity detectable in local field potential recordings in hippocampal area CA1.  $\sim$ 50-150 ms-long events are referred to as 'sharp wave-ripples' (SWRs) (Colgin, 2016; Fernández-Ruiz et al., 2019), and they occur during non-locomotor periods of quiet wakefulness, during reward consumption, and during slow-wave sleep, when sensory information about the spatial environment is reduced or absent. During SWRs, sparse subsets of neurons are co-activated, with a tendency for neurons that fire sequentially during exploratory behaviour to also fire sequentially during SWRs, either in the same order, or in reverse, or with a mixture of both directions (Davidson et al., 2009; Pfeiffer, 2020; Stella et al., 2019; Wu & Foster, 2014). The hippocampus can also activate sequences of place cells during SWRs that correspond to possible paths through the environment that have not actually been experienced, suggesting a possible role for offline sequence generation in behavioural planning (Gupta et al., 2010; Igata et al., 2021; Ólafsdóttir et al., 2015, 2018; Wu & Foster, 2014). Manipulations that disrupt neuronal activity during SWRs result in deficits in memory recall (Girardeau et al., 2009; Jadhav et al., 2012), supporting a hypothesis that offline reactivation of neuronal ensembles during SWRs is important for the maintenance and consolidation of long-term memories (Buzsáki, 1989; Joo & Frank, 2018).

Hippocampal SWRs are thought to be generated by the synchronous firing of subpopulations of neurons in the CA2 and CA3 regions of the hippocampus (Csicsvari et al., 2000; Oliva et al., 2016), which are characterized by substantial recurrent feedback connectivity (Duigou et al., 2014; Guzman et al., 2016; Okamoto & Ikegaya, 2019). Recurrent networks have long been appreciated for their ability to generate rich internal dynamics (Amit & Brunel, 1997), including oscillations (Ermentrout, 1992). It has also been shown that associative plasticity at recurrent connections between excitatory neurons can enable robust reconstruction of complete memory representations from incomplete or noisy sensory cues (Amit & Brunel, 1997; Griniasty et al., 1993; Guzman et al., 2016; Hopfield, 1982; Marr, 1971; Treves & Rolls, 1994). However, this 'pattern completion' function of recurrent networks requires that similarly tuned neurons activate each other via strong synaptic connections, resulting in sustained self-activation, rather than sequential activation of neurons that are selective for distinct stimuli (Lisman et al., 2005; Pfeiffer & Foster, 2015; Renno-Costa et al., 2014). Previous work has shown that, in order for recurrent networks to generate sequential activity, some mechanism must be in place to 'break the symmetry' and enable spread of activity from one ensemble of cells to another (Sompolinsky & Kanter, 1986; Tsodyks et al., 1996). During spatial navigation, feedforward sensory inputs carrying information about the changing environment can provide the momentum necessary for sequence generation. However, during hippocampal SWRs, sensory inputs are reduced, and activity patterns are thought to be primarily internally generated by the recurrent connections within the hippocampus. In this study we use a computational model of hippocampal area CA3 to investigate the synaptic, cellular and network mechanisms that enable flexible offline generation of memory-related neuronal sequences in the absence of ordered sensory information.

A number of possible mechanisms for sequence generation in recurrent networks have been proposed:

- (1) Winner-takes-all network mechanism (Almeida et al., 2007, 2009a; Lisman & Jensen, 2013). Within this framework, the subset of excitatory neurons receiving the most strongly weighted synaptic inputs responds first upon presentation of a stimulus. This active ensemble of cells then recruits feedback inhibition via local interneurons, which in turn prevents other neurons from firing for a brief time window (e.g. the  $\sim$ 15 ms duration of a single gamma cycle). This highlights the important roles that inhibitory neurons play in regulating sparsity (how many cells are co-active), selectivity (which cells are active) and rhythmicity (when cells fire) in recurrent networks (Almeida et al., 2009b; Rennó-Costa et al., 2019; Stark et al., 2014; Stefanelli et al., 2016). However, while oscillatory feedback inhibition provides a network mechanism for parsing neuronal sequences into discrete elements, additional mechanisms are still required to ensure that distinct subsets of excitatory neurons are activated in a particular order across successive cycles of a rhythm (Lisman et al., 2005; Ramirez-Villegas et al., 2018).
- (2) Heterogeneous cellular excitability (Luczak et al., 2007; Stark et al., 2015). If the intrinsic properties of neurons in a network are variable and heterogeneous, when a stimulus is presented, those neurons that are the most excitable will fire early, while neurons with progressively lower excitability will fire later, resulting in sequence generation. This mechanism can explain the offline generation of stereotyped, unidirectional sequences, but cannot account for variable generation of sequences in both forward and reverse directions.
- (3) Asymmetric distributions of synaptic weights (Sompolinsky & Kanter, 1986; Tsodyks et al., 1996). During learning, if changes in synaptic weights are controlled by a temporally asymmetric learning rule, recurrent connections can become biased such that neurons activated early in a sequence have stronger connections onto neurons activated later

in a sequence (Levy, 1989; Malerba & Bazhenov, 2019; McNaughton & Morris, 1987; Reifenstein et al., 2021). This enables internally generated activity to flow along the direction of the bias in synaptic weights. While this mechanism accounts for offline replay of specific sequences in the same order experienced during learning, it cannot account for reverse replay or the flexible generation of non-experienced sequences (Gupta et al., 2010; Igata et al., 2021; Ólafsdóttir et al., 2015, 2018; Wu & Foster, 2014).

(4) Cellular or synaptic adaptation. It has also been proposed that short-term adaptation of either neuronal firing rate (Ecker et al., 2022; Itskov et al., 2011; Treves, 2004) or synaptic efficacy (Romani & Tsodyks, 2015) can enable neuronal sequence generation in recurrent networks without asymmetric synaptic weights. According to this scheme, recently activated neurons initially recruit connected partners with high efficacy, but continued spiking results in either a decrease in firing rate or a decrease in the probability of neurotransmitter release. This causes connections to fatigue over time, and favours the sequential propagation of activity to more recently activated cells. These mechanisms do allow for the stochastic generation of neuronal sequences in either the forward or reverse direction, though they do not prescribe which or how many neurons will participate in a given replay event.

In this study, we sought to understand how neuronal sequence generation in hippocampal area CA3 depends on the structure and function of the underlying network. To do this, we constructed a computational neuronal network model comprising recurrently connected excitatory and inhibitory spiking neurons, and tuned it to match experimental constraints on the spiking dynamics of CA3 during spatial navigation, including sparsity, selectivity, rhythmicity and spike rate adaptation. We then analysed the direction and content of neuronal sequences generated both 'online' during simulated navigation, and 'offline' during simulated rest. We found that when the network was driven by ordered sensory information in the online state, it generated forward-sweeping 'theta sequences' that depended on the structure of recurrent connectivity in the network. In the offline state driven by noise, the network generated heterogeneous memory replay events that moved in either forward, or reverse, or mixed directions, and depended on network sparsity and rhythmicity, and neuronal stimulus selectivity and spike-rate adaptation. Model degeneracy analysis and network perturbations indicated that offline memory replay does not occur in networks with disrupted recurrent connectivity, or in networks lacking sparsity, selectivity, rhythmicity, or spike rate adaptation. Finally, when particular spatial locations were over-represented by the network, as occurs in the hippocampus at sites of reward (Lee et al., 2006; Turi et al., 2019; Zaremba et al., 2017), memory replay events were biased towards trajectories that included those salient positions (Gillespie et al., 2021; Ólafsdóttir et al., 2015; Singer & Frank, 2009).

### **Methods**

## **Ethical approval**

No animal or human subjects were used in this study. This research was performed in compliance with all institutional policies regarding ethical research practices.

# **Neuronal network modelling**

Simulations of a recurrent network of excitatory and inhibitory spiking neurons were executed using the Python interface for the NEURON simulation software (Hines et al., 2009). Cell models were single-compartment integrate-and-fire neuronal cell models, as defined by Izhikevich (2007), and as implemented for the NEURON simulator by Lytton et al. (2016). Previously calibrated cell models were replicated from those previous reports without modification - the 'intrinsically bursting cell' model was used for excitatory neurons (E) with spike rate adaptation, the 'regular spiking pyramidal cell' model was used for excitatory neurons without spike rate adaptation, and the 'fast-spiking interneuron' model was used for inhibitory neurons (I) (Izhikevich, 2007; Lytton et al., 2016). Individual spikes in presynaptic neurons activated saturable conductance-based synapses with exponential rise and decay kinetics after a constant delay of 1 ms to emulate axonal conduction time (Carnevale & Hines, 2006). Excitatory synapses had a reversal potential of 0 mV (like AMPA-type glutamate receptors), and inhibitory synapses had a reversal potential of -80 mV (like GABA<sub>A</sub>-type receptors). In addition to the excitatory (E) and inhibitory (I) neuron populations, a population of feedforward afferent inputs (FF) provided a source of external excitatory synaptic drive to the model network.

4697793, 2023, 15, Downloaded from https://physoc.onlinelibrary.wiley.com/doi/10.1113/P283216, Wiley. Online Library on [29/02/2024]. See the Terms and Conditions (https://onlinelibrary.wiley.com/terms-and-conditions) on Wiley Online Library for rules of use; OA articles are governed by the applicable Certain Commons License

The baseline weights of excitatory synapses onto E cells were sampled from a log-normal distribution (Almeida et al., 2009b; Buzsaki & Mizuseki, 2014), while the weights of excitatory synapses onto I cells, and all inhibitory synapses were sampled from a normal distribution (Grienberger et al., 2017). In addition to the random baseline synaptic weights assigned to excitatory synapses onto E cells, input strengths were increased by a variable additive factor that depended on the distance between the place fields of cells with overlapping spatial selectivity (Supplementary Fig. S1B). The place field locations of the FF and E populations were assigned by distributing

Table 1. Model parameter values

Parameter	Bounds	Structured $E \leftarrow E$ weights	$\begin{array}{c} Random \\ E \leftarrow E \\ weights \end{array}$	Shuffled $E \leftarrow E$ weights	Suppressed rhythmicity	No sparsity or selectivity constraints	No spike rate adaptatior
E ← FF weight mean	0.1–5	1.28	0.29	1.30	0.37	1.57	0.55
$E \leftarrow FF$ weight st. dev.	0.1–5	1.09	0.21	0.91	0.80	0.88	0.41
E ← E weight mean	0.1–5	0.75	0.50	1.43	0.90	0.54	2.45
$E \leftarrow E$ weight st. dev.	0.1–5	0.52	0.48	0.58	0.25	0.73	1.74
$E \leftarrow I$ weight mean	0.1–5	0.87	0.70	2.06	0.86	0.59	0.54
$E \leftarrow I$ weight st. dev.	0.1–5	0.47	0.32	0.41	0.76	0.73	0.16
I ← FF weight mean	0.1–5	1.50	1.83	2.44	0.38	1.53	1.60
$I \leftarrow FF$ weight st. dev.	0.1–5	0.68	0.82	0.45	0.38	0.55	0.22
I ← E weight mean	0.1–5	1.85	1.31	1.44	1.63	1.77	0.82
$I \leftarrow E$ weight st. dev.	0.1–5	0.22	0.28	0.21	0.17	0.14	0.79
I ← I weight mean	0.1–5	0.16	1.07	0.26	2.51	0.15	0.23
$I \leftarrow I$ weight st. dev.	0.1–5	0.12	0.68	0.47	0.33	0.77	0.05
$E \leftarrow FF \ and \ E \leftarrow E \ max$ structured $\Delta weight$	1–5	3.63	2.80	4.42	3.91	3.63	4.00
$E \leftarrow FF$ and $E \leftarrow E$ decay (ms)	2-20	3.43	10.76	3.48	19.87	3.53	5.91
$E \leftarrow I \text{ decay (ms)}$	2-30	2.32	3.89	2.72	17.05	2.53	27.87
$I \leftarrow FF \text{ and } I \leftarrow E \text{ decay (ms)}$	2–20	15.04	18.53	17.94	13.49	17.10	18.39
$I \leftarrow I \text{ decay (ms)}$	2-30	8.09	5.65	8.12	9.24	10.19	22.35
$E \leftarrow FF$ no. synapses/pair	0–2	0.62	0.96	0.70	0.57	0.73	0.18
$E \leftarrow E$ no. synapses/pair	0–2	0.55	0.57	0.55	0.05	0.33	0.46
$E \leftarrow I \text{ no. synapses/pair}$	0–10	5.12	3.36	4.75	7.93	5.71	7.79
I ← FF no. synapses/pair	0–2	0.26	0.77	0.19	0.21	0.19	0.12
I ← E no. synapses/pair	0–2	0.31	0.47	0.19	0.22	0.13	0.60
I ← I no. synapses/pair	0–10	8.17	4.81	9.07	8.83	9.43	7.38

locations throughout the circular simulated track at equal intervals and randomly assigning them to cells within each population. Random connectivity resulted in each E neuron receiving inputs from many FF and E neurons with heterogeneous selectivity, which produced substantial out-of-field excitation at all positions along the track.

For each of six types of connections between the three cell types (E  $\leftarrow$  FF, E  $\leftarrow$  E, E  $\leftarrow$  I, I  $\leftarrow$  FF, I  $\leftarrow$  E, I  $\leftarrow$  I), a number of parameters were varied and explored during optimization to identify model configurations that produced dynamics comparable to experimental observations. These parameters included: the mean and variance of the synaptic weight distribution for each connection type, the decay time constants of the synaptic conductances, the mean number of synapses made by one presynaptic cell onto one postsynaptic cell for each pair of cell types, and the maximum increase in synaptic weight due to shared selectivity, as mentioned above. Self-connections were not permitted.

Optimization was performed using a population-based iterative multi-objective algorithm. During each of 50 iterations, a population of 600 models with different parameters were simulated for one trial of simulated online run, and for 5 trials of simulated offline rest. During offline rest trials, a random subset of 25% of feed-

forward inputs were active with a mean rate of 12.5 Hz for an event duration of 160 ms (8 bins of 20 ms each). Different trials were implemented by using a distinct random number stream to sample unique spike times of the feedforward inputs from an inhomogeneous Poisson process. The following features of the network dynamics were evaluated for each model: average minimum and maximum firing rates of E cells during run, average mean firing rates of I cells during run, average fraction of active E and I cells during run, mean firing rates of E cells during rest, average fraction of active E cells during rest, and finally, features related to the frequency and power of theta and gamma band oscillations in E and I cells during run. These features were compared to target values to obtain a set of multiple objective error values. Models within a population were compared to each other and ranked with a non-dominated sorting procedure (Deb, 2011). Then, a new population of models was generated by making small perturbations to the parameter values of the most highly ranked models from the previous iteration. This algorithm effectively identified model configurations that satisfied multiple objective criteria. In Tables 1 and 2, the final optimized parameter values (Table 1) and measured features of the network dynamics (Table 2) are compared for various model configurations discussed in this study.

Table 2. Features of model network dynamics

Feature	Target	Structured $E \leftarrow E$ weights	$\begin{array}{c} Random \\ E \leftarrow E \\ weights \end{array}$	Shuffled $E \leftarrow E$ weights	Suppressed rhythmicity	No sparsity or selectivity constraints	No spike rate adaptation
E peak rate (run) (Hz)	20.	17.20	19.96	10.42	20.07	19.73	7.30
E min rate (run) (Hz)	0.	0.24	0.25	0.27	0.25	12.37	0.39
I mean rate (run) (Hz)	20.	19.58	32.05	12.08	2.77	19.90	6.17
E fraction active (run)	0.6	0.59	0.60	0.61	0.60	1.00	0.60
I fraction active (run)	0.95	1.00	1.00	0.95	0.23	0.98	0.87
E theta amplitude (run)	0.5	0.78	0.37	0.63	0.15	0.77	1.29
I theta amplitude (run)	0.5	0.48	0.14	0.19	0.26	0.53	1.15
E gamma amplitude (run)	0.25	0.53	0.40	0.66	0.20	0.59	0.27
I gamma amplitude (run)	0.25	1.19	1.85	1.33	1.67	1.39	1.27
E theta frequency (run) (Hz)	7.	7.09	7.45	7.64	11.27	7.09	6.73
I theta frequency (run) (Hz)	7.	6.91	7.27	7.45	12.55	6.91	6.73
E gamma frequency (run) (Hz)	70.	71.06	72.93	71.06	57.98	72.93	39.29
I gamma frequency (run) (Hz)	70.	71.06	72.93	69.19	87.88	76.67	69.19
E theta frequency tuning index (run)	>5.	6.40	6.30	7.00	0.00	29.05	150.67
I theta frequency tuning index (run)	>5.	9.83	6.10	3.99	0.00	34.16	150.59
E gamma frequency tuning index (run)	>5.	10.67	10.90	5.08	-0.37	10.18	-0.01
I gamma frequency tuning index (run)	>5.	16.16	4.14	31.65	0.36	6.02	3.43
E fraction active (rest)	0.25	0.37	0.20	0.53	0.36	1.00	0.40
E mean rate (rest) (Hz)	12.5	7.11	6.56	7.12	7.65	17.77	6.97

In Tables 1 and 2, theta and gamma amplitudes were quantified as follows. Average population firing rates were band-pass filtered, and the envelopes of the filtered traces were computed from the Hilbert transformation. Then power was expressed as a ratio of the average envelope amplitude to the average population firing rate. To quantify theta and gamma frequency, bandpass filtered traces were subject to frequency decomposition, and the frequency corresponding to the centroid or centre-of-mass of the power spectral density distribution was taken as the dominant frequency within the band. The area of the power spectral density distribution was also used to compute a 'frequency tuning index' which quantified how concentrated the power distribution was around the centroid frequency. This metric was akin to a signal-to-noise ratio in the frequency domain instead of the time domain, and was computed as follows:

$$FTI = \frac{S - N}{2 \times \sigma \times w} \tag{1}$$

where S is the average power at frequencies within the centre of mass quartile containing the centroid frequency (signal), N is the average power at frequencies in the extreme high and low quartiles outside the centre of mass quartile (noise),  $\sigma$  is the standard deviation of the

power distribution, and w is the half-width of the power distribution in the frequency domain normalized to the width of the bandpass filter. This metric has values near zero when power is distributed uniformly within the filter band, and values larger than 1 when power is concentrated around the centroid frequency.

4697793, 2023, 15, Downloaded from https://physoc.onlinelibrary.wiley.com/doi/10.1113/JP283216, Wiley Online Library on [29/022024]. See the Terms and Conditions (https://onlinelibrary.wiley.com/terms-and-conditions) on Wiley Online Library for rules of use; OA articles are governed by the applicable Certain Commons License

Following parameter optimization, each variant of the network was evaluated by simulating five trials of online run, and 1000 trials of offline rest for each of five independent network instances. For a given set of model parameters, independent instances of each network variant were constructed by using distinct random number streams to assign place field locations, input spike times, synaptic connections and synaptic weights for all cells in the network.

Bayesian decoding of spatial position from spike times recorded during a single trial (Figs 2, 3, 5 and 6, and Supplementary Figs S3–S6) was performed using the procedure described in Davidson et al. (2009). The spatial firing rates of all cells were averaged across five trials of simulated online run to compute the spiking probabilities of each neuron in 20 ms bins. Then, spiking data were taken from either a held-out set of five trials of simulated run (Fig. 2), or offline rest trials (Figs 3, 5 and 6, and Supplementary Figs S3–S6). The numbers of spikes emitted by each cell in 20 ms bins were used to

determine a likelihood distribution over spatial positions. The position with maximum likelihood was used as the decoded position estimate for each temporal bin. In Fig. 2A, decoded positions of E and I cells sweep smoothly from past to future positions, and then relax back to the current position on the timescale of the ongoing theta rhythm. To quantify this form of online neuronal sequence generation, a theta sequence score (Figs 2E and 4H) was computed as follows: decoded position error was first bandpass filtered in the theta band (4-10 Hz). Then the contribution of this oscillation to the total variance in decoded position error was calculated as the square of the correlation  $(R^2)$  between the original mean-subtracted error signal and the theta filtered signal. In Figs 3F, M, 4I, 5G and 6G, and Supplementary Figs S3H, S4F, S5K, S6K and S8E, offline sequences were categorized as consistent with a continuous trajectory through space if they met the following criteria: (1) at least one cell in a population must emit at least one spike in each temporal bin, (2) the change in decoded position between any two adjacent bins must not exceed 35% of the track length, (3) the total path length of the decoded trajectory must not exceed 100% of the track length, and (4) the net speed of the trajectory (absolute value of net change in position divided by the 160 ms offline event duration) must exceed 50% of the run speed of 0.33 track lengths/s used during simulation of online exploration.

In Fig. 4 and Supplementary Fig. S8, the diversity and degeneracy of various model configurations was explored as follows: for each model configuration, 30,000 models were evaluated during parameter optimization, and the model with the lowest multi-objective error score was considered the 'best' model. The remaining models were sorted by their Euclidean distance from the 'best' model in the space of model parameters. This resulted in an error landscape (e.g. Fig. 4A) in which models with similar parameters resulted in similar multi-objective error scores. We then identified models located at local minima in this error landscape, which as a group comprised models that were distant from each other in parameter space, but similar to each other in terms of overall multi-objective error. We further enforced that selected models had to be a minimum distance of 0.15 from each other in parameter space, and selected five such models with the lowest error score to be included in a 'Marder group' of models for further analysis. For each alternative network model configuration (i.e. network models with and without structured recurrent excitatory connections), each of five 'Marder group' model variants with different parameters were evaluated for offline sequence generation by simulating 1000 trials for each of five independent network instances.

In box and whisker plots in Figs 2D, E, 3F, M, 4D–I, 5G and 6G, and Supplementary Figs S1C, D, S3H, S4F, S5K, S6K and S8A–E, centre lines indicate median, boxes span

the first and third quartile of the data, and whiskers extend to 1.5 times the inter-quartile range.

#### **Statistics**

Differences in mean values between cell populations (e.g. E vs. FF) across n = 5 instances of a single variant (e.g. 'best' model) of a single network model configuration (e.g. model with structured recurrent excitatory synaptic weights in Fig. 1) were evaluated with a one-sided paired Student's t test. Differences in mean values for one cell population between two model configurations (n = 5 instances each from a single model variant) (e.g. structured weights vs. random weights in Fig. 2) were evaluated with two-sided t tests. Differences in the distributions of data across trials either between two model configurations or between cell populations for a single model configuration (n=5instances each from a single model variant) were evaluated using the Kolmogorov-Smirnov (K-S) test. Differences in mean values between two model configurations across n=5 model variants (data averaged over five instances of each variant) were evaluated using two-sided t tests. P-values were adjusted for multiple comparison using the Bonferonni method for small numbers of comparisons, and using the Benjamini-Hochberg method to reduce false discovery rate (FDR) for large numbers of comparisons.

# **Results**

To investigate how sequential activity in the hippocampus generated 'online' during spatial exploration can be recapitulated 'offline' in the absence of sensory cues, we constructed a simple spiking neuronal network model of rodent hippocampal area CA3 (Methods). Neural circuits in the hippocampus and cortex typically comprise a majority of excitatory neurons that project information to downstream circuits, and a minority of primarily locally connected inhibitory interneurons. We included populations of excitatory (1000) and inhibitory (200) neurons in proportion to experimental observations (Pelkey et al., 2017; Tremblay et al., 2016) (Fig. 1A). Cell models were single-compartment, integrate-and-fire neurons with saturable, conductance-based excitatory and inhibitory synapses (Carnevale & Hines, 2006; Izhikevich, 2007; Izhikevich & Edelman, 2008). Excitatory neurons were endowed with spike-rate adaptation to support punctuated bursting behaviour during theta oscillations (O'Keefe & Recce, 1993; Scharfman, 1993), and inhibitory neurons exhibited fast-spiking dynamics to sustain continuous high frequency firing during gamma oscillations (Csicsvari et al., 2003; Ylinen et al., 1995) (Supplementary Fig. S1A, Methods).

To simulate the sensory experience of locomotion in a spatial environment, we provided both excitatory and inhibitory neurons with external afferent inputs from a population of 1000 excitatory neurons, each of which was selectively activated at distinct but overlapping positions within a simulated circular track that took 3 s to traverse (Fig. 1A–C, Methods). Recurrent connections within and between excitatory and inhibitory cell populations were also included (Fig. 1A), as they are hallmark features of

hippocampal area CA3, and have been shown to support rich network dynamics (Renno-Costa et al., 2014; Stark et al., 2014). Specifically, inhibitory feedback connections have been shown to regulate the number of simultaneously active neurons (sparsity) (Stefanelli et al., 2016), and to contribute to the generation of theta and gamma network oscillations (Bezaire et al., 2016; Geisler et al., 2005; Rennó-Costa et al., 2019; Stark et al., 2014; Wang, 2010). Plastic excitatory connections between excitatory neurons

14697793, 2023, 15, Downloaded from https://phtysoc.onlinelibrary.wiley.com/doi/10.1113/JP283216, Wiley Online Library on [29/02/2024]. See the Terms and Conditions (https://onlinelibrary.wiley.com/terms-and-conditions) on Wiley Online Library for rules of use; OA articles are governed by the applicable Cerative Commons Licensean Conditions (https://onlinelibrary.wiley.com/terms-and-conditions) on Wiley Online Library for rules of use; OA articles are governed by the applicable Cerative Commons Licensean Conditions (https://onlinelibrary.wiley.com/terms-and-conditions) on Wiley Online Library for rules of use; OA articles are governed by the applicable Cerative Commons Licensean Conditions (https://onlinelibrary.wiley.com/terms-and-conditions) on Wiley Online Library for rules of use; OA articles are governed by the applicable Cerative Commons Licensean Conditions (https://onlinelibrary.wiley.com/terms-and-conditions) on Wiley Online Library for rules of use; OA articles are governed by the applicable Cerative Commons Licensean Conditions (https://onlinelibrary.wiley.com/terms-and-conditions) on Wiley Online Library for rules of use; OA articles are governed by the applicable Cerative Commons Licensean Conditions (https://onlinelibrary.wiley.com/terms-and-conditions) on Wiley Online Library for rules of use; OA articles are governed by the applicable Cerative Commons (https://onlinelibrary.wiley.com/terms-and-conditions) on the articles are governed by the applicable Cerative Commons (https://onlinelibrary.wiley.com/terms-and-conditions) on the articles are governed by the applicable Cerative Commons (https://onlinelibrary.wiley.com/terms-and-conditions) on the articles are governed by the applicable Cerative Commons (https://onlinelibrary.wiley.com/terms-and-conditions) on the articles are governed by the applicable Cerative Commons (https://onlinelibrary.wiley.com/terms-and-conditions) on the articles are governed by the ar

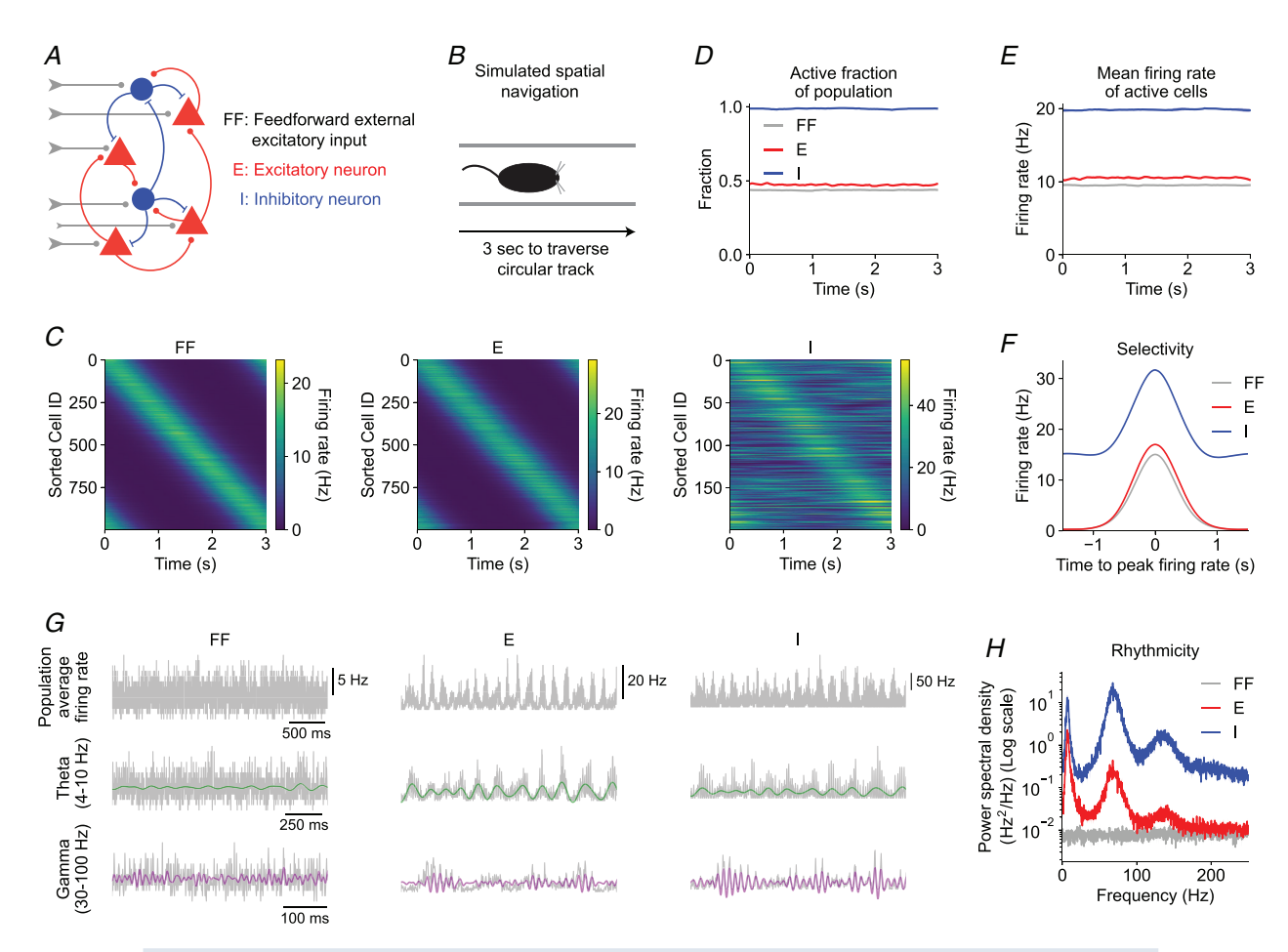


Figure 1. Sparsity, selectivity, and rhythmicity in a recurrent spiking neuronal network model of hippocampal area CA3

A, diagram illustrating connectivity of network model. Feedforward (FF) external excitatory inputs contact excitatory (E) and inhibitory (I) neurons. E and I neurons are recurrently connected to other E and I neurons. B. simulations of rodent 'online exploration' emulating the response of the hippocampus during unidirectional locomotion along a circular linear track that takes 3 s to traverse at constant run velocity. C, firing rates vs. time of all neurons in each cell population (average of five trials from one example network instance). Cells in each population are sorted by the location of maximum firing. D, population sparsity (active fraction of neurons) vs. time shown for each cell population. E, mean firing rate of active neurons vs. time shown for each cell population. F, average stimulus selectivity of each cell population. Trial-averaged activity of each cell was centred around the location of maximum firing, and then averaged across cells. G, the average activity of each population on a single trial (top row) was bandpass filtered in the theta (middle row) and gamma (bottom row) frequency bands. Coloured traces show filtered signals (theta: green, gamma: purple). Traces derived from one example network instance. H, power spectrum of average population activity indicates dominant frequency components in the theta and gamma bands (one-sided paired t tests: theta: E vs. FF, P=0.00001; I vs. FF, P < 0.00001; gamma: E vs. FF, P < 0.00001; I vs. FF, P < 0.00001). In C, D, F and H, data were first averaged across five trials per network instance. Means (continuous line)  $\pm$  SEM (shading) were computed across five independent instances of each network model. P-values reflect FDR correction for multiple comparisons.

have long been implicated in stimulus selectivity and the storage and recall of memories (Almeida et al., 2007; Hopfield, 1982; Lisman & Jensen, 2013). It has been proposed that strong connections between ensembles of co-active neurons could arise through a combination of biased connectivity during brain development (Buzsáki et al., 2021; Dragoi & Tonegawa, 2013; Farooq & Dragoi, 2019; Grosmark & Buzsáki, 2016), and experience-driven synaptic plasticity during learning (Bittner et al., 2015, 2017; Brunel & Trullier, 1998; Káli & Dayan, 2000; Milstein et al., 2021; O'Neill et al., 2008). While here we did not simulate these dynamic processes explicitly, we implemented the structured connectivity that is the end result of these processes by increasing the strengths of synaptic connections between excitatory cells that share overlapping selectivity for spatial positions in the environment (Table 1, Supplementary Fig. S1B, Methods) (Arkhipov et al., 2018).

Despite the relatively simple architecture of this network model, a wide range of networks with distinct dynamics could be produced by varying a number of parameters, including (1) the probabilities of connections between cell types (Káli & Dayan, 2000), (2) the kinetics and strengths of synaptic connections between cell types (Brunel & Wang, 2003), and (3) the magnitude of the above-mentioned increase in synaptic strengths between neurons with shared selectivity (Brunel, 2016; Dorkenwald et al., 2019). To calibrate the network model to produce dynamics that matched experimentally derived targets, we performed an iterative stochastic search over these parameters (see Methods, Table 1 for complete list of parameters), and optimized the following features of the activity of the model network: (1) population sparsity - the fraction of active neurons of each cell type, (2) the mean firing rates of active neurons of each cell type, (3) stimulus-selective firing of excitatory cells, and (4) the frequency and amplitude of theta and gamma oscillations in the synchronous spiking activity of each cell population (Methods).

This procedure identified a model with dynamics that met all of the above constraints. Given sparse and selective feedforward inputs during simulated navigation (Fig. 1B and C), the excitatory neurons in the network responded with a fraction of active cells (Fig. 1D) and with average firing rates comparable to the those of the feedforward input population (Fig. 1E). The majority of inhibitory neurons were activated continuously (Fig. 1C and D) at high firing rates (Fig. 1E). While excitatory neurons received random connections from feedforward afferents and from other excitatory neurons with heterogeneous spatial tuning, excitatory cells exhibited a high degree of spatial selectivity (Fig. 1C and F). This selective increase in firing rate at specific spatial locations within the 'place field' of each excitatory neuron was supported by enhanced synaptic connection strengths between excitatory neurons with overlapping tuning (Supplementary Fig. S1B). While substantial background excitation occurred in all cells at all spatial positions, firing outside the place field of each cell was suppressed by sufficiently strong inhibitory input (Bittner et al., 2015; Grienberger et al., 2017). Interestingly, inhibitory neurons also exhibited spatial selectivity, albeit to a weaker degree and with a higher background firing rate (Fig. 1*C* and *F*). This feature of the network dynamics was an emergent property that was not explicitly designed or optimized. While excitatory connections onto inhibitory cells were random and not weighted according to shared selectivity (Supplementary Fig. S1B), the total amount of excitatory input arriving onto individual inhibitory cells fluctuated across spatial positions, and predicted a small degree of spatial selectivity (Supplementary Fig. S1C). Inhibitory inputs received by inhibitory cells reduced their average activity, effectively enabling fluctuations in excitation above the mean to stand out from the background excitation (Supplementary Fig. S1C and D). This mechanism of background subtraction by inhibitory synaptic input may explain the partial spatial selectivity previously observed in subpopulations of hippocampal inhibitory neurons (Ego-Stengel & Wilson, 2007; Geiller et al., 2020; Grienberger et al., 2017; Hangya et al., 2010; Marshall et al., 2002; Wilent & Nitz, 2007).

The tuned network model also exhibited oscillatory synchrony in the firing of the excitatory and inhibitory neuron populations, despite being driven by an asynchronous external input (Fig. 1G and H). The requirement that the network self-generate rhythmic activity in the theta band constrained recurrent excitatory connections to be relatively strong, as this input provided the only source of rhythmic excitation within the network (Supplementary Fig. S1*E*). Interestingly, as the firing rates of inhibitory cells increased within each cycle of the theta rhythm, their synchrony in the gamma band increased, resulting in an amplitude modulation of gamma paced at the theta frequency (Fig. 1G and Supplementary Fig. S1F). This 'theta-nested gamma' is a well-known feature of oscillations in the hippocampus (Soltesz & Deschenes, 1993; Ylinen et al., 1995), and here emerged from fundamental constraints on dual band rhythmicity without requiring additional mechanisms or tuning.

# Position decoding reveals 'theta sequences' during simulated navigation

Next, we analysed neuronal sequence generation within the network during simulated navigation. First, we simulated multiple trials and computed trial-averaged spatial firing rate maps for all neurons in the network (Fig. 1*C*). We then used these rate maps to perform Bayesian decoding of spatial position given the spiking

activity of all cells in the network from individual held-out trials not used in constructing the decoding template (Fig. 2A, Methods) (Davidson et al., 2009; Zhang et al., 1998). For the population of feedforward excitatory inputs, the underlying spatial firing rates were imposed, and the spikes of each cell were generated by sampling from an inhomogeneous Poisson process. Thus, decoding position from the activity of this population served to validate our decoding method, and indeed simulated position could be decoded from the spiking activity of the feedforward input population with very low reconstruction error (Fig. 2A and D). When we applied this method to the population of excitatory neurons within the network, reconstruction error was increased (Fig. 2A and D). This reflected an increased fraction of temporal bins (20 ms) where the decoded position was either behind or in advance of the actual position (Fig. 2A). However, rather than simply reflecting reconstruction noise or poor spatial selectivity of individual cells (Fig. 1F), these divergences from actual position resulted from consistent sequential structure in the spiking activity of cells in the excitatory population (Fig. 2A, bottom row). Ordered neuronal firing resulted in decoded positions that continuously swept from past positions, through the current actual position, to future positions, and then reset to past positions, on the timescale of the ongoing theta rhythm. These 'theta sequences' caused decoded position estimates to oscillate around the actual position (Fig. 2A, bottom row), and this theta timescale oscillation accounted for a large proportion of the variance in decoded position (Fig. 2E, Methods). Interestingly, we found that position could also be accurately decoded from the moderately spatially tuned activity of inhibitory cells in the network (Fig. 2A and D), and that the spiking activity of the inhibitory population was also organized into theta sequences (Fig. 2A, bottom row and E).

A number of possible mechanisms have been proposed to account for theta sequence generation in vivo, including synaptic, cell-intrinsic and network-level mechanisms (Chadwick et al., 2015, 2016; Drieu & Zugaro, 2019; Foster & Wilson, 2007; Grienberger et al., 2017; Kang & DeWeese, 2019; Mehta et al., 2002; Skaggs et al., 1996). That theta sequences in the model emerged in both excitatory and inhibitory neuron populations implicates recurrent interactions within the network (Chadwick et al., 2016). To further investigate, we analysed neuronal sequence generation in a variant of the model in which the strengths of recurrent connections between excitatory neurons were randomized and no longer depended on shared spatial selectivity between connected pairs of cells (Supplementary Fig. S2A). This alternative model could still be tuned to match experimental targets, including sparsity, selectivity and rhythmicity (Supplementary Fig. S2B–F). In this case the spatial selectivity of excitatory cells was entirely determined by the synaptic weights of the feedforward afferent inputs (Supplementary Fig. S2A), while the recurrent excitatory input supported synchronization in the theta and gamma bands (Supplementary Fig. S2F). However, in this model, theta timescale neuronal sequence generation in both excitatory and inhibitory cells was suppressed (Fig. 2B and E). Decoding of position from spikes on single trials produced lower reconstruction error (Fig. 2D), as neuronal population activity more faithfully followed the current spatial position provided by the feedforward inputs, and was not organized into the sweeps from past to future positions characteristic of theta sequences (Fig. 2B, bottom row and E). We also tested a related variant of the model in which the skewed distribution of recurrent excitatory synaptic weights used in the structured weights model (Figs 1 and 2A, and Supplementary Fig. 1) was randomly shuffled (Fig. 2C and Supplementary Fig. S2G-L). Theta sequence generation was also reduced in this network model variant (Fig. 2*E*). These results indicate that structure in the synaptic strengths of recurrent excitatory connections is required for the generation of fast timescale (~125 ms) neuronal sequences when network activity is driven by behavioural timescale (>1 s) sequences of sensory inputs, as occurs during spatial exploration.

# **Emergence of offline memory replay**

The above results show that the same network structure that enables population dynamics in CA3 to exhibit sparsity, selectivity, and rhythmicity also supports neuronal sequence generation in the online state when ordered sensory information is present. We next sought to understand how neuronal sequences consistent with the sensory environment are generated offline when sensory inputs are reduced. To mimic the transient ( $\sim$ 50-150 ms) increase in population activity that occurs during a hippocampal SWR (Fernández-Ruiz et al., 2019), we transiently stimulated the network by randomly choosing sparse subsets of cells from the feedforward input population to emit spikes (Fig. 3A and B). We then used the same decoding templates as above, constructed from the trial-averaged activity during simulated run, to decode spatial position from spiking activity during these transient offline events (Methods).

4697793, 2023, 15, Downloaded from https://physoc.onlinelibrary.wiley.com/doi/10.1113/JP283216, Wiley Online Library on [29/022024]. See the Terms and Conditions (https://onlinelibrary.wiley.com/terms-and-conditions) on Wiley Online Library for rules of use; OA articles are governed by the applicable Certain Commons License

Given that the place field locations of the stimulated neurons in the feedforward input population were heterogeneous and unordered, the spatial positions decoded from their spiking were typically discontiguous across adjacent temporal bins (Fig. 3A, B and F). This input pattern evoked spiking in sparse subsets of both the excitatory and the inhibitory populations in the network (Fig. 3A and B). In contrast with the feedforward

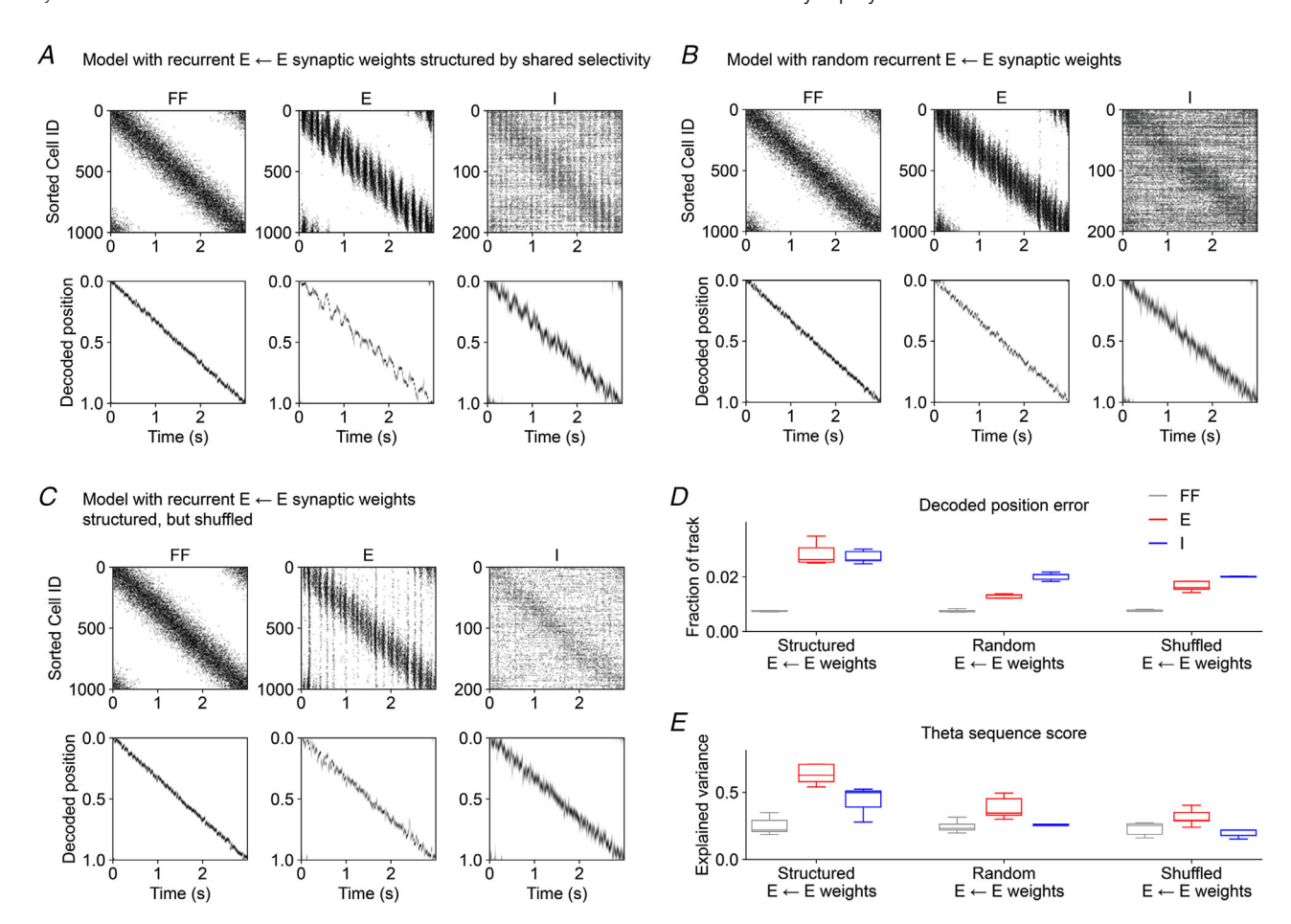


Figure 2. Online neuronal sequence generation depends on recurrent excitatory synaptic connectivity A, 'online exploration' was simulated for the same network model as in Fig. 1, in which recurrent excitatory connections between E cells were structured such that neurons with shared selectivity have elevated synaptic weights. Top row: spike times of all neurons in each cell population on a single trial of simulated 'online exploration' are marked. A separate set of five trials was used to construct a spatial firing rate template for each neuron (shown in Fig. 1C). Cells in each population are sorted by the location of maximum average spatial firing rate. Bottom row: the spatial firing rate templates for all neurons were used to perform Bayesian decoding of spatial position from the single trial spiking data shown in the top row. For each cell population, the likelihood of each spatial position in each time bin (20 ms) is indicated by grayscale intensity. B, same as A for alternative network model with random synaptic strengths at recurrent excitatory connections between E cells. Spatial firing rate templates used for decoding are shown in Supplementary Fig. S2B. C, same as A for alternative network model in which the structured excitatory recurrent synaptic weights between E cells were randomly shuffled. Spatial firing rate templates used for decoding are shown in Supplementary Fig. S2H. D, decoded position error is quantified as the difference between actual and predicted position. The absolute value of decoded position error is expressed as a fraction of the track length (one-sided paired t tests: structured  $E \leftarrow E$  weights: E vs. FF, P < 0.00001; I vs. FF, P < 0.00001; random E  $\leftarrow$  E weights: E vs. FF, P = 0.00001; I vs. FF, P = 0.00001; shuffled E  $\leftarrow$  E weights: E vs. FF, P = 0.00001; I vs. FF, P = 0.00001; two-sided t tests vs. data from model with structured E  $\leftarrow$  E weights: random E  $\leftarrow$  E weights: E, P < 0.00001, I, P = 0.00001; shuffled E  $\leftarrow$  E weights: E, P < 0.00001, I, P = 0.00001). E, in the model with structured  $E \leftarrow E$  weights, decoded positions of E and I cell populations oscillated between past, current and future positions at the timescale of the population theta oscillation. A theta sequence score was computed as the proportion of the variance in the decoded position error explained by a theta timescale oscillation (see Methods) (one-sided paired t tests: structured E  $\leftarrow$  E weights: E vs. FF, P = 0.00005; I vs. FF, P = 0.00005; random E  $\leftarrow$  E weights: E vs. FF, P = 0.00002; I vs. FF, P = 0.28287; shuffled E  $\leftarrow$  E weights: E vs. FF, P = 0.00010; I vs. FF, P = 0.99600; two-sided t tests vs. data from model with structured E  $\leftarrow$  E weights: random E  $\leftarrow$  E weights: E, P < 0.00001, I, P < 0.00001; shuffled E  $\leftarrow$  E weights: E, P < 0.00001, I, P < 0.00001). In (D) and (E), data were first averaged across five trials per network instance. Box and whisker plots depict data from five independent instances of each network model (see Methods). P-values reflect FDR correction for multiple comparisons.

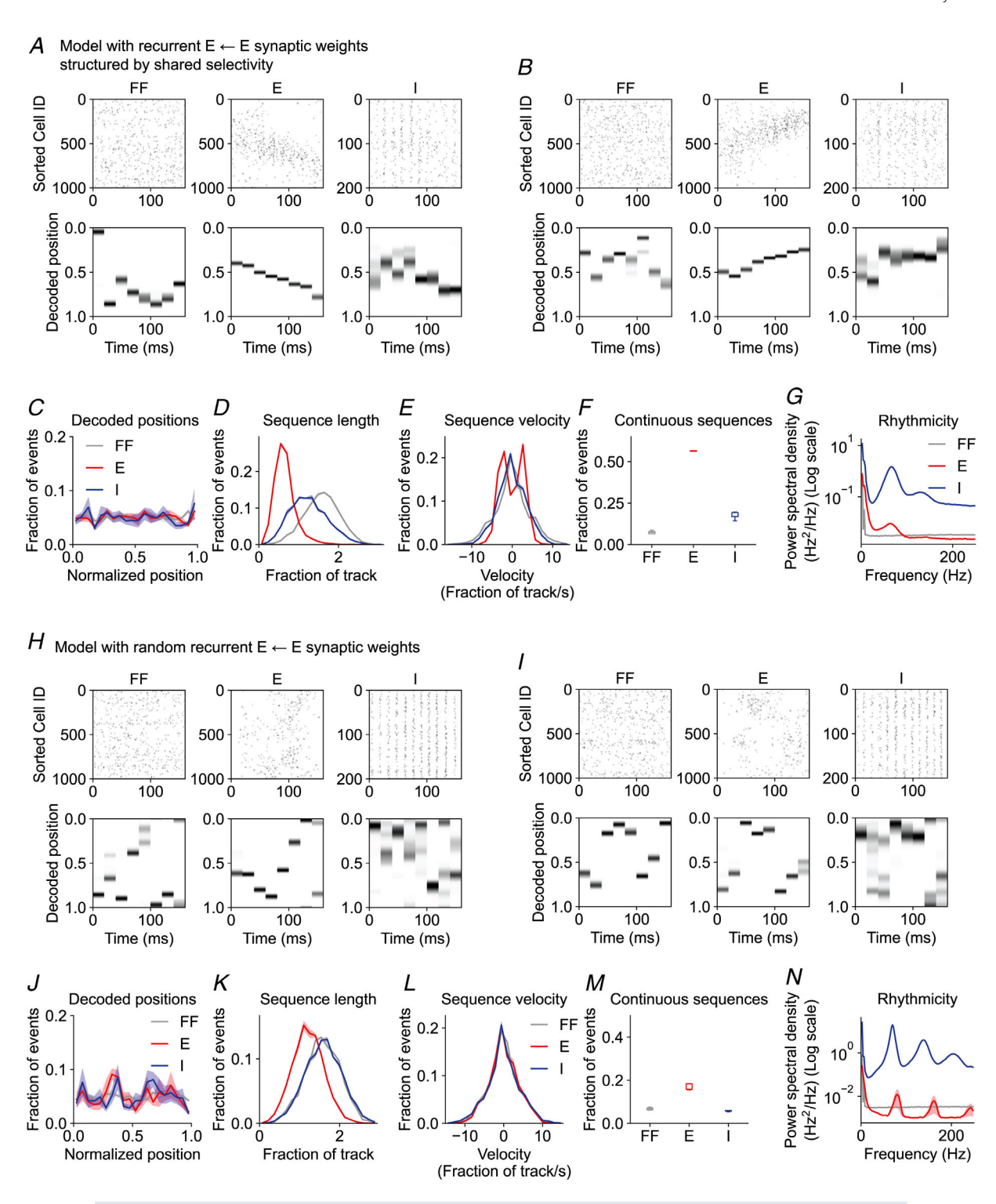


Figure 3. Forward and reverse offline memory replay depends on recurrent excitatory synaptic connectivity

A–B, 'offline rest' was simulated for the network model with structured  $E \leftarrow E$  weights (Fig. 1). Top row: spike times of all neurons in each cell population on a single trial of simulated 'offline rest' are marked. Data from five trials of simulated 'online exploration' were used to construct a spatial firing rate template for each neuron (Fig. 1C). Cells in each population are sorted by the location of maximum average spatial firing rate. Bottom row: the spatial firing rate templates for all neurons were used to perform Bayesian decoding of spatial position from the single trial spiking data shown in the top row. For each cell population, the likelihood of each spatial position in each time bin (20 ms) is indicated by grayscale intensity. A and B correspond to two example trials from one example network

14697793, 2023, 15, Downloaded from https://phtysoc.onlinelibrary.wiley.com/doi/10.1113/JP283216, Wiley Online Library on [29/02/2024]. See the Terms and Conditions (https://onlinelibrary.wiley.com/terms-and-conditions) on Wiley Online Library for rules of use; OA articles are governed by the applicable Cerative Commons Licensean Conditions (https://onlinelibrary.wiley.com/terms-and-conditions) on Wiley Online Library for rules of use; OA articles are governed by the applicable Cerative Commons Licensean Conditions (https://onlinelibrary.wiley.com/terms-and-conditions) on Wiley Online Library for rules of use; OA articles are governed by the applicable Cerative Commons Licensean Conditions (https://onlinelibrary.wiley.com/terms-and-conditions) on Wiley Online Library for rules of use; OA articles are governed by the applicable Cerative Commons Licensean Conditions (https://onlinelibrary.wiley.com/terms-and-conditions) on Wiley Online Library for rules of use; OA articles are governed by the applicable Cerative Commons Licensean Conditions (https://onlinelibrary.wiley.com/terms-and-conditions) on Wiley Online Library for rules of use; OA articles are governed by the applicable Cerative Commons Licensean Conditions (https://onlinelibrary.wiley.com/terms-and-conditions) on Wiley Online Library for rules of use; OA articles are governed by the applicable Cerative Commons (https://onlinelibrary.wiley.com/terms-and-conditions) on the articles are governed by the applicable Cerative Commons (https://onlinelibrary.wiley.com/terms-and-conditions) on the articles are governed by the applicable Cerative Commons (https://onlinelibrary.wiley.com/terms-and-conditions) on the articles are governed by the applicable Cerative Commons (https://onlinelibrary.wiley.com/terms-and-conditions) on the articles are governed by the applicable Cerative Commons (https://onlinelibrary.wiley.com/terms-and-conditions) on the articles are governed by the ar

instance. C-G, this procedure was repeated for 1000 trials for each of five instances of the network. C, histogram of spatial positions decoded from each cell population across all simulated replay events (two-sided K-S tests: E vs. FF, P = 0.99974; I vs. FF, P = 0.99974).  $D_r$  histogram of the path length of spatial sequences decoded from each cell population (two-sided K-S tests: E vs. FF, P < 0.00001; I vs. FF, P < 0.00001). E, histogram of the mean velocity of spatial sequences decoded from each cell population (two-sided K-S tests: E vs. FF, P = 0.00235; I vs. FF, P = 0.73515). F, fraction of events that met criterion for sequences consistent with continuous spatial trajectories (see Methods) (one-sided paired t tests: E vs. FF, P < 0.00001, I vs. FF, P = 0.00084). G, power spectrum of average population activity indicates high frequency components (one-sided paired t tests: 75–300 Hz frequency band: E vs. FF, P = 1; I vs. FF, P < 0.00001). H-N, same as A-G for an alternative network model with random  $E \leftarrow E$  weights. H and I correspond to two example trials from one example network instance. J, decoded positions (two-sided K-S tests: E vs. FF, P = 0.99974; I vs. FF, P = 0.99974; two-sided K-S tests vs. data from model with structured E  $\leftarrow$  E weights in C: E, P = 0.85869; I, P = 0.87577). K, offline sequence path length (two-sided K-S tests: E vs. FF, P < 0.00001; I vs. FF, P = 0.99997; two-sided K-S tests vs. data from model with structured E  $\leftarrow$  E weights in D: E, P < 0.00001; I, P < 0.00001). L, offline sequence velocity (two-sided K-S tests: E vs. FF, P = 0.99877; I vs. FF, P = 0.99877; two-sided K-S tests vs. data from model with structured E  $\leftarrow$  E weights in (E): E, P = 0.01591; I, P = 0.76837). M, fraction of events that met criterion for sequences consistent with continuous spatial trajectories (see Methods) (one-sided paired t tests; E vs. FF. P = 0.00005. I vs. FF. P = 0.86564; two-sided t tests vs. data from model with structured E  $\leftarrow$  E weights in (F): E, P < 0.00001; I, P = 0.00001). N, offline high-frequency rhythmicity (one-sided paired t tests: 75–300 Hz frequency band: E vs. FF, P = 0.97708; I vs. FF, P < 0.00001; two-sided t tests vs. data from model with structured E  $\leftarrow$  E weights in G: E, P = 0.64948; I, P < 0.00001). In C-E, G, J-L, and N, means (continuous line)  $\pm$  SEM (shading) were computed across five independent instances of each network. In F and M, box and whisker plots depict data from five independent instances of each network model (see Methods). P-values reflect FDR correction for multiple comparisons.

population, the activity evoked in excitatory neurons was structured such that neurons with nearby place field locations spiked in adjacent temporal bins, resulting in decoded spatial trajectories that were continuous (Fig. 3A, B and F). Inhibitory neuron activity during these events was organized into high-frequency oscillations (Fig. 3A, B and G). This procedure was repeated to produce thousands of offline events evoked by stimulation of different random ensembles of inputs (Methods). Across these events, each position along the track was decoded with equal probability (Fig. 3C). For each event, the length and mean velocity of the decoded trajectory was calculated from the differences in decoded positions between adjacent bins (Fig. 3D and E). A mean velocity of zero corresponds to events with equal steps in the forward and reverse directions, while positive velocities correspond to net forward-moving trajectories, and negative velocities correspond to net backwards-moving trajectories. While the trajectories decoded from the random feedforward input population comprised large, discontiguous steps that traced out large path lengths with an average velocity near zero, the excitatory neuron population generated shorter, more continuous sequences that progressed in either the forward or reverse directions (Fig. 3D–F). These trajectories on average covered  $\sim$ 0.5 of the length of the track in the short ( $\sim$ 150 ms) duration of the offline event. Compared to the run trajectory, which took 3 s to cover the full track length, this corresponded to a ~10-fold temporal compression (Fig. 3E), similar to experimental data (Davidson et al., 2009). Spatial trajectories decoded from the inhibitory neuron population were intermediate in length, but with little forward or reverse momentum, similar to the feedforward inputs. However, the inhibitory cells exhibited

high-frequency synchrony (Fig. 3A, B and G), similar to experimentally recorded CA3 interneurons during hippocampal SWRs (Csicsvari et al., 2000; Tukker et al., 2013).

These data demonstrate that random, unstructured input can evoke sequential activity in a CA3-like recurrent spiking network, with sequences corresponding to forward, reverse, or mixed direction trajectories through an experienced spatial environment. This self-generated memory-related activity implicates information stored in the synaptic weights of the recurrent connections within the network as being important for offline replay of experience. However, in most previous models, sequence generation was unidirectional, and was enabled by an asymmetric bias in the strengths of recurrent connections such that neurons encoding positions early in a sequence formed stronger synapses onto neurons encoding later positions (Levy, 1989; Malerba & Bazhenov, 2019; McNaughton & Morris, 1987; Reifenstein et al., 2021; Sompolinsky & Kanter, 1986; Tsodyks et al., 1996). In contrast, the current network flexibly generated sequences in forward, reverse or mixed directions, and had symmetric recurrent connections such that synaptic strengths between pairs of excitatory neurons depend only on overlapping selectivity, not on sequence order. Does sequence generation in the present network still depend on recurrent connectivity? To test this, we first verified that including an asymmetric bias in the strengths of excitatory connections produced offline replay events that were biased towards forward sequences (Supplementary Fig. S3). We next analysed the sequence content of offline events generated in the variants of the network model with random (Fig. 3H-N and Supplementary Fig. S2A-F) or shuffled Supplementary Fig. S2G-L and S4)

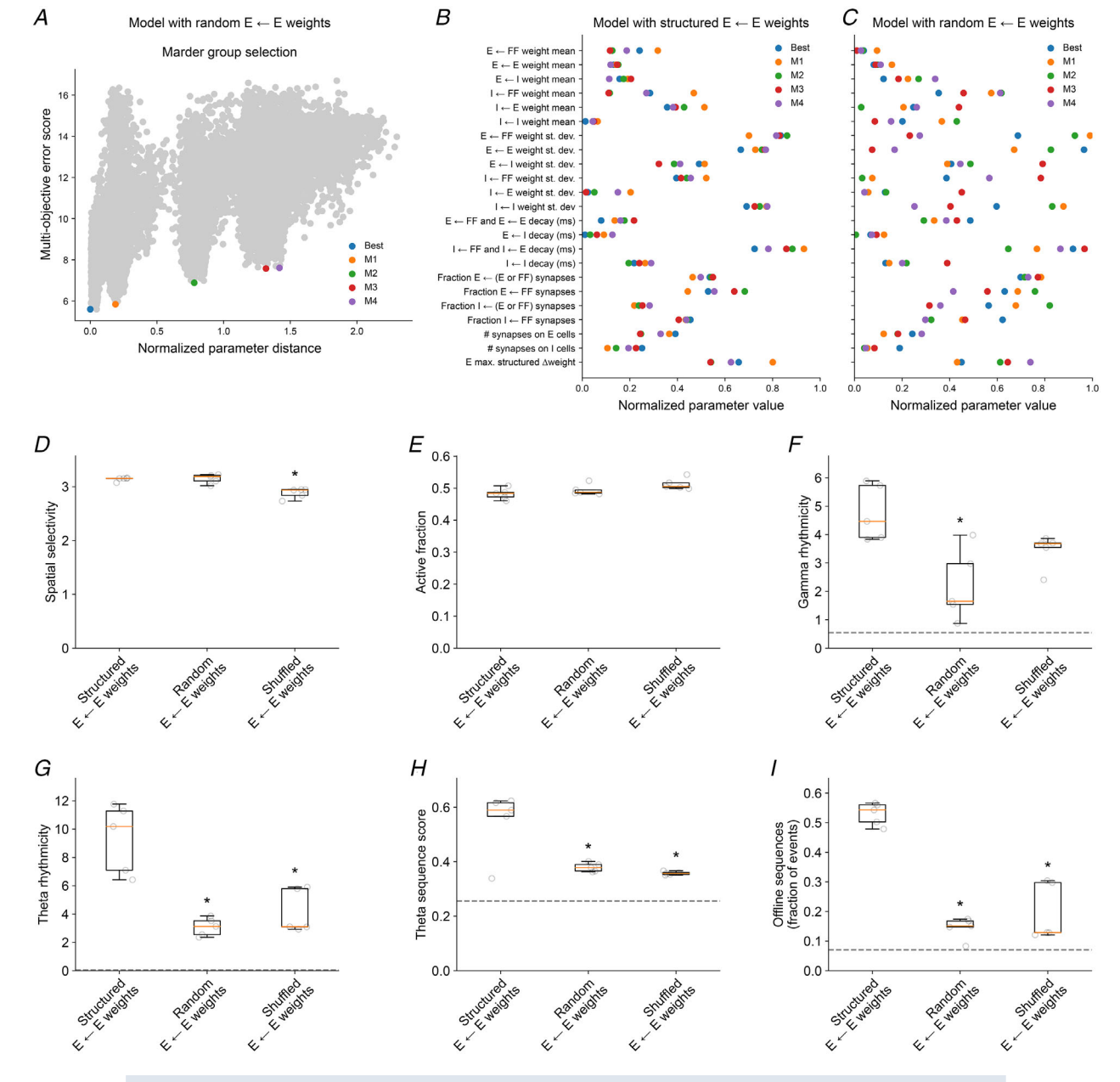


Figure 4. Exploration of model parameter diversity and degeneracy

A. during network model optimization, 30,000 model variants with different parameters were evaluated. To explore model diversity and degeneracy, for each network model configuration, a subset of model variants termed a 'Marder group' were selected based on their large distance from each other in the space of parameters, but their similar performance with respect to multiple optimization objectives (see Methods). This selection procedure is illustrated here for the model with random  $E \leftarrow E$  weights as an example. The five 'Marder group' members with the lowest multi-objective error (labelled 'best' and 'M1'-'M4') were selected for further evaluation. B, for the network model configuration with structured  $E \leftarrow E$  weights, the range of parameter values across five distinct 'Marder group' models is shown. C, same as B for the model with random  $E \leftarrow E$  weights. D-I, features of the simulated network dynamics produced by distinct model variants within a 'Marder group' are compared across network model configurations. Each data point (grey circles) depicts one 'Marder group' model. D, spatial selectivity of the excitatory neuron population during simulated 'online exploration' is computed as a ratio of maximum to mean activity (two-sided t tests vs. data from model with structured  $E \leftarrow E$  weights: random  $E \leftarrow E$  weights: P = 1; shuffled E  $\leftarrow$  E weights: P = 0.00224). E, the fraction of the excitatory neuron population that is synchronously active during simulated 'online exploration' is shown (two-sided t tests vs. data from model with structured  $E \leftarrow$ E weights: random E  $\leftarrow$  E weights: P = 1; shuffled E  $\leftarrow$  E weights: P = 0.12079). F, gamma rhythmicity of the excitatory neuron population is computed as the integrated power spectral density in the gamma frequency band (two-sided t tests vs. data from model with structured E  $\leftarrow$  E weights: random E  $\leftarrow$  E weights: P = 0.03552;

14697793, 2023, 15, Downloaded from https://phtysoc.onlinelibrary.wiley.com/doi/10.1113/JP283216, Wiley Online Library on [29/02/2024]. See the Terms and Conditions (https://onlinelibrary.wiley.com/terms-and-conditions) on Wiley Online Library for rules of use; OA articles are governed by the applicable Cerative Commons Licensean Conditions (https://onlinelibrary.wiley.com/terms-and-conditions) on Wiley Online Library for rules of use; OA articles are governed by the applicable Cerative Commons Licensean Conditions (https://onlinelibrary.wiley.com/terms-and-conditions) on Wiley Online Library for rules of use; OA articles are governed by the applicable Cerative Commons Licensean Conditions (https://onlinelibrary.wiley.com/terms-and-conditions) on Wiley Online Library for rules of use; OA articles are governed by the applicable Cerative Commons Licensean Conditions (https://onlinelibrary.wiley.com/terms-and-conditions) on Wiley Online Library for rules of use; OA articles are governed by the applicable Cerative Commons Licensean Conditions (https://onlinelibrary.wiley.com/terms-and-conditions) on Wiley Online Library for rules of use; OA articles are governed by the applicable Cerative Commons Licensean Conditions (https://onlinelibrary.wiley.com/terms-and-conditions) on Wiley Online Library for rules of use; OA articles are governed by the applicable Cerative Commons (https://onlinelibrary.wiley.com/terms-and-conditions) on the articles are governed by the applicable Cerative Commons (https://onlinelibrary.wiley.com/terms-and-conditions) on the articles are governed by the applicable Cerative Commons (https://onlinelibrary.wiley.com/terms-and-conditions) on the articles are governed by the applicable Cerative Commons (https://onlinelibrary.wiley.com/terms-and-conditions) on the articles are governed by the applicable Cerative Commons (https://onlinelibrary.wiley.com/terms-and-conditions) on the articles are governed by the ar

shuffled  $E \leftarrow E$  weights: P = 0.16364). G, theta rhythmicity of the excitatory neuron population is computed as the integrated power spectral density in the theta frequency band (two-sided t tests vs. data from model with structured  $E \leftarrow E$  weights: random  $E \leftarrow E$  weights: P = 0.00272; shuffled  $E \leftarrow E$  weights: P = 0.01944). H, theta sequence score (see Fig. 2 and Methods) (two-sided t tests vs. data from model with structured  $E \leftarrow E$  weights: random  $E \leftarrow E$  weights: P = 0.02817; shuffled  $E \leftarrow E$  weights: P = 0.01473).  $E \leftarrow E$ , fraction of events during simulated 'offline rest' that met criterion for sequences consistent with continuous spatial trajectories (see Fig. 3, Supplementary Fig. S3 and Methods) (two-sided  $E \leftarrow E$  weights:  $E \leftarrow E$ 

recurrent connection weights. Indeed, without structure in the recurrent connection weights, spatial trajectories decoded from the activity of excitatory neurons was more similar to those of the feedforward inputs, consisting of large, discontinuous steps without forward or reverse momentum (Fig. 3H–M and Supplementary Fig. S4A–F). Still, these networks exhibited high-frequency oscillatory synchrony during these offline events (Fig. 3N and Supplementary Fig. S4G).

# **Exploration of model diversity and degeneracy**

The above results strongly supported the hypothesis that recurrent connectivity is important for offline sequence generation. During optimization of each of the alternative network model configurations shown above to meet the multiple objectives of sparsity, selectivity and rhythmicity, we evaluated 30,000 variants of each model with different parameters (Methods). For each model configuration, the model with the lowest overall multi-objective error was chosen as the 'best' model for further analysis, as shown in Figs 2 and 3 and Supplementary Figs S1, S2 and S4. However, we noted that the parameter values that specified these 'best' models were variable across the multiple network configurations (Table 1). This raised the possibility that while many models with diverse parameters may produce networks with similar online dynamics (referred to as model degeneracy; Marder & Taylor, 2011), perhaps only a smaller subset of models would additionally support the emergence of offline sequence generation. The fact that sequence generation was not observed for either of the 'best' models with disrupted recurrent excitatory synaptic weights could reflect an incomplete sampling of the parameter space and a failure to identify models that both meet the objective criteria for online dynamics and produce offline sequences. Therefore, in order to explore the diversity and degeneracy of models evaluated during optimization, we devised a method to identify models that performed similarly with respect to multiple optimization objectives, but were specified by divergent sets of parameters (Methods). For each model configuration, all model variants evaluated during parameter optimization were sorted by their Euclidean distance from the 'best' model in the space of model parameters. This resulted in an error landscape (e.g. Fig. 4A) in which models with similar parameters resulted in similar multi-objective error scores. We then identified models located at local minima in this error landscape, which formed a group of models that were distant from each other in parameter space, but similar to each other in terms of overall multi-objective error. We termed a set of such models as a 'Marder group' after pioneering work characterizing degeneracy in biological systems (Marder & Taylor, 2011). For each alternative network model configuration, we selected the five members of this 'Marder group' with the lowest multi-objective error (labelled 'best' and 'M1'-'M4' in Fig. 4A), and evaluated their network dynamics during simulations of both online exploration and offline rest. We first verified that for all model configurations with and without structured recurrent excitatory connectivity analysed above (Figs 1-3 and Supplementary Figs S1, S2 and S4), model variants within a 'Marder group' exhibited considerable diversity across model parameters (Fig. 4B and C), and met all objective criteria for neuronal stimulus selectivity (Fig. 4D), population sparsity (Fig. 4E), and rhythmogenesis in the theta and gamma bands (Fig. 4*F* and *G*). However, only model variants with synaptic weights structured by shared stimulus selectivity exhibited theta sequences during online run (Fig. 4H) and generated offline sequences consistent with continuous spatial trajectories (Fig. 41). This analysis demonstrated that generation of memory-related neuronal sequences by recurrent networks requires that information about the topology of the sensory environment is stored in the strengths of recurrent excitatory connections between excitatory neurons.

# Constraints on online sparsity, selectivity and rhythmicity enable offline memory replay

Our above findings suggest that experimental constraints on the online dynamics of hippocampal area CA3 during spatial exploration are sufficient to enable the emergence of offline memory replay. We next sought to determine whether all or only a subset of these constraints were required for generation of memory-related sequences. To determine the importance of rhythmicity, we removed the optimization criteria that excitatory and inhibitory neuron populations synchronize in the theta and gamma bands, and instead added an objective to minimize power density across the full frequency spectrum (Supplementary Fig. S5E). Following optimization, this alternative network model exhibited reduced rhythmicity, but still met objectives related to sparsity and selectivity (Supplementary Fig. S5A-D). However, when challenged with random stimuli during simulated offline rest, this model with suppressed rhythmicity failed to generate continuous forward or reverse sequences (Supplementary Fig. S5F-L). Rather, spatial trajectories decoded from offline population activity contained large discontiguous jumps in position, and most events had zero net velocity in either the forward or the reverse direction. This indicated that the same reciprocal interactions between excitatory and inhibitory neurons that support rhythmogenesis in the theta and gamma bands also contribute to the sequential organization of neuronal activity during offline memory replay.

We next optimized a network model variant without constraints on population sparsity and neuronal stimulus selectivity (see Methods). In this network model, while feedforward excitatory inputs remained spatially tuned, their connectivity with excitatory neurons was shuffled to prevent inheritance of spatial selectivity. This resulted in a complete loss of sparsity of excitatory neuron activity (Supplementary Fig. S6A and B), and suppressed stimulus selectivity in excitatory neurons even below the level exhibited in the inhibitory neuron population (Supplementary Fig. S6C and D). Rhythmogenesis in the theta and gamma bands in excitatory and inhibitory neurons was maintained (Supplementary Fig. S6E). During simulation of offline rest, this network generated highly synchronous population bursts that tended to either hover at one decoded position or make large discontiguous jumps between positions (Supplementary Fig. S6F-K). These results suggest that the network connectivity parameters that support highly sparse and selective neuronal activity in the online stimulus-driven state, also enable sparse reactivation of neuronal sequences in the offline state. We also repeated the model degeneracy analysis described above (Fig. 4) for multiple model variants with compromised sparsity, selectivity or rhythmicity, which corroborated these findings (Supplementary Fig. S8).

# Role of neuronal spike rate adaptation in forward and reverse offline memory replay

Above we showed that structure in the synaptic connectivity of the CA3 network is important for

neuronal sequence generation. However, unlike previous models of sequence generation where asymmetry in connection strengths biased the direction of neuronal sequences (Levy, 1989; Malerba & Bazhenov, 2019; McNaughton & Morris, 1987; Reifenstein et al., 2021; Sompolinsky & Kanter, 1986; Tsodyks et al., 1996), here synaptic connectivity was symmetric, and yet variable neuronal sequences were flexibly generated in both forward and reverse directions (Fig. 3A, B and E). If this symmetric connectivity enables recurrent networks to generate either forward or backward steps, what 'breaks' this symmetry and produces sequences that make net progress in either the forward or backward direction? We next wondered if directionality of offline sequences in our network model was facilitated by our choice of 'bursty' excitatory cell model, which exhibited spike-rate adaptation (Fig. 5A). As mentioned before, use-dependent decreases in either firing rate or synaptic transmission over time can provide momentum to neuronal sequences by favouring the recruitment of new neurons that have not yet been activated during a network population event (Itskov et al., 2011; Romani & Tsodyks, 2015; Treves, 2004). To test a possible role for cellular adaptation in sequence generation in our model network, we replaced the 'bursting' excitatory cell model with a 'regular spiking' model without spike rate adaptation (Fig. 5A). This cell model did not support the high instantaneous firing rates of the bursting cell model, which compromised the peak firing rates of excitatory cells in the network and their entrainment by higher frequency gamma oscillations during simulated online navigation (Supplementary Fig. S7). Otherwise, this variant of the network did meet the criterion for sparsity, selectivity and rhythmicity (Supplementary Figs S7 and S8A-D). However, during simulated offline rest, random feedforward inputs evoked a truncated response from the network (Fig. 5B and C), with the high frequency rhythmic activity of the inhibitory neurons diminishing before the end of the stimulus period (Fig. 5B, C and H). Spatial trajectories decoded from the activity of excitatory neurons in the network comprised large steps that did not progress in either forward or reverse direction, similar to the random feedforward inputs (Fig. 5E-G and Supplementary Fig. S8E). These data show that adaptation of neuronal spiking provides a cellular-level mechanism for flexible and reversible sequence generation in recurrent spiking networks.

4697793, 2023, 15, Downloaded from https://physoc.onlinelibrary.wiley.com/doi/10.1113/P283216, Wiley. Online Library on [29/02/2024]. See the Terms and Conditions (https://onlinelibrary.wiley.com/terms-and-conditions) on Wiley Online Library for rules of use; OA articles are governed by the applicable Certain Commons License

# Preferential replay of reward location

Thus far, we have simulated network activity during spatial navigation, and identified features of the network that enable offline replay of behavioural sequences stored in memory. However, in these simulations all spatial positions were visited with equal occupancy,

4697793, 2023, 15, Downloaded from https://physoc.onlinelibrary.wiley.com/doi/10.1113/P283216, Wiley. Online Library on [29/02/2024]. See the Terms and Conditions (https://onlinelibrary.wiley.com/terms-and-conditions) on Wiley Online Library for rules of use; OA articles are governed by the applicable Certain Commons License

and considered to be of equal salience or relevance to the virtual animal. This resulted in all positions being replayed with equal probability offline (Fig. 3*C*), mimicking experimental conditions where all spatial positions contain discriminable sensory cues, and opportunities

for reward are provided at random times and positions (Turi et al., 2019; Zaremba et al., 2017). However, it has been shown that when a reward is provided at a fixed location that the animal must discover through learning, offline memory replay events become biased towards

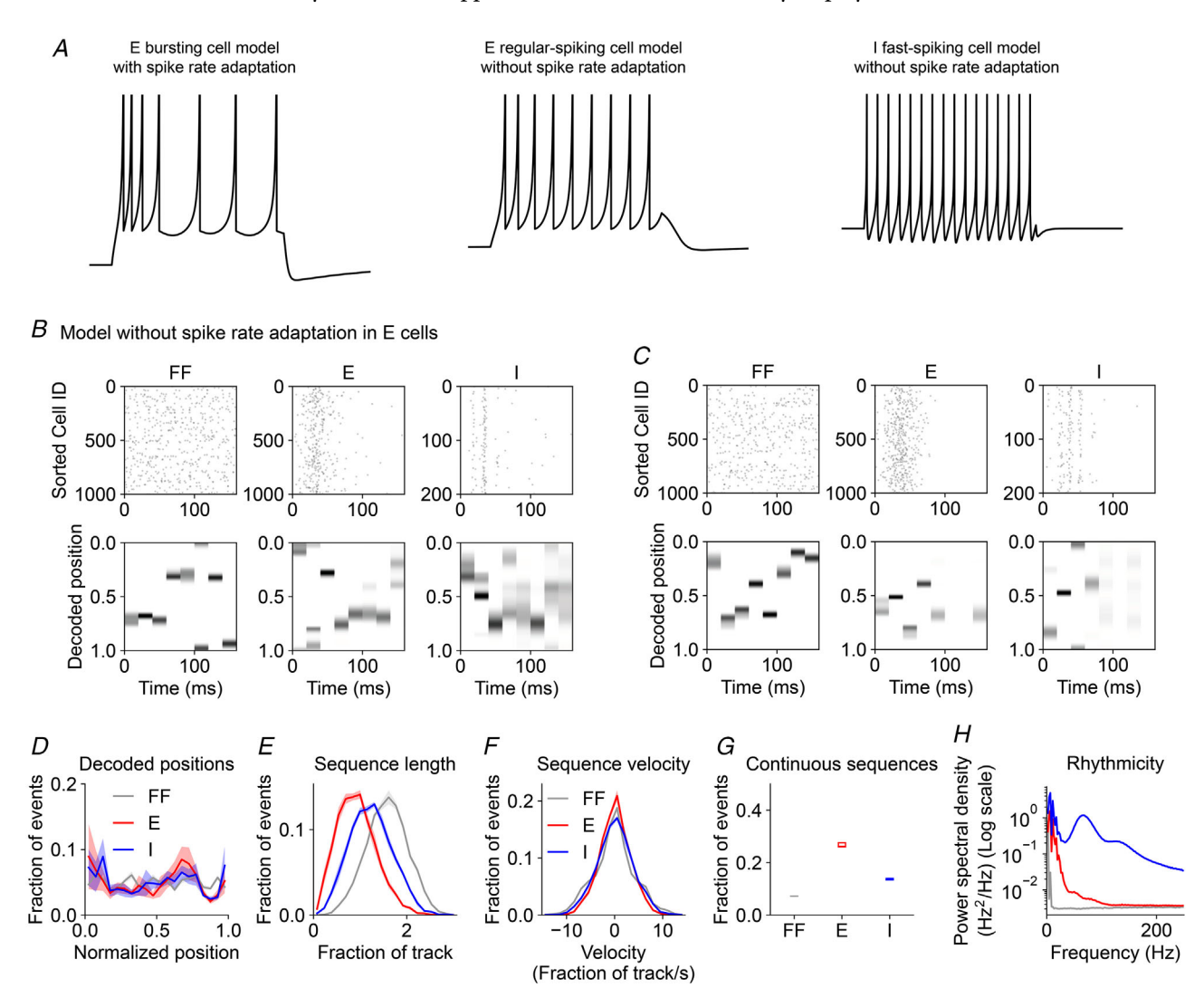


Figure 5. Neuronal spike rate adaptation supports offline memory replay

A, intracellular voltage recordings of three neuronal cell models with distinct spiking dynamics in response to simulated square-shaped intracellular current injections. B-H, same as Figs 3A-2G for an alternative network model in which E cells are regular-spiking cell models without spike rate adaptation. B and C correspond to two example trials from one example network instance. D, decoded positions (two-sided K-S tests: E vs. FF, P = 0.99974; I vs. FF, P = 0.89825; two-sided K-S tests vs. data from model with structured E  $\leftarrow$  E weights in Fig. 3C: E, P = 0.84875; I, P = 0.85869). E, offline sequence length (two-sided K-S tests: E vs. FF, P < 0.00001; I vs. FF, P < 0.00001; two-sided K-S tests vs. data from model with structured  $E \leftarrow E$  weights in Fig. 3D: E, P < 0.00001; I, P = 0.99997). F, offline sequence velocity (two-sided K-S tests: E vs. FF, P = 0.15282; I vs. FF, P = 0.73515; two-sided K-S tests vs. data from model with structured E  $\leftarrow$  E weights in Fig. 3E: E, P = 0.03099; I, P = 0.91017). G, fraction of events that met criterion for sequences consistent with continuous spatial trajectories (see Methods) (one-sided paired t tests: E vs. FF, P = 0.00038, I vs. FF, P = 0.00119; two-sided t tests vs. data from model with structured E  $\leftarrow$  E weights in Fig. 3F: E, P < 0.00001; I, P = 0.03860). H, offline high-frequency rhythmicity (one-sided paired t tests: 75–300 Hz frequency band: E vs. FF, P = 0.00114; I vs. FF, P = 0.00003; two-sided t tests vs. data from model with structured E  $\leftarrow$  E weights in Fig. 3G: E, P < 0.00001; I, P = 0.00027). In D-F and H, means (continuous lines)  $\pm$  SEM (shading) were computed across five independent instances of each network. In G, box and whisker plots depict data from five independent instances of each network model (see Methods). P-values reflect FDR correction for multiple comparisons.

### A Model with population over-representation of reward location

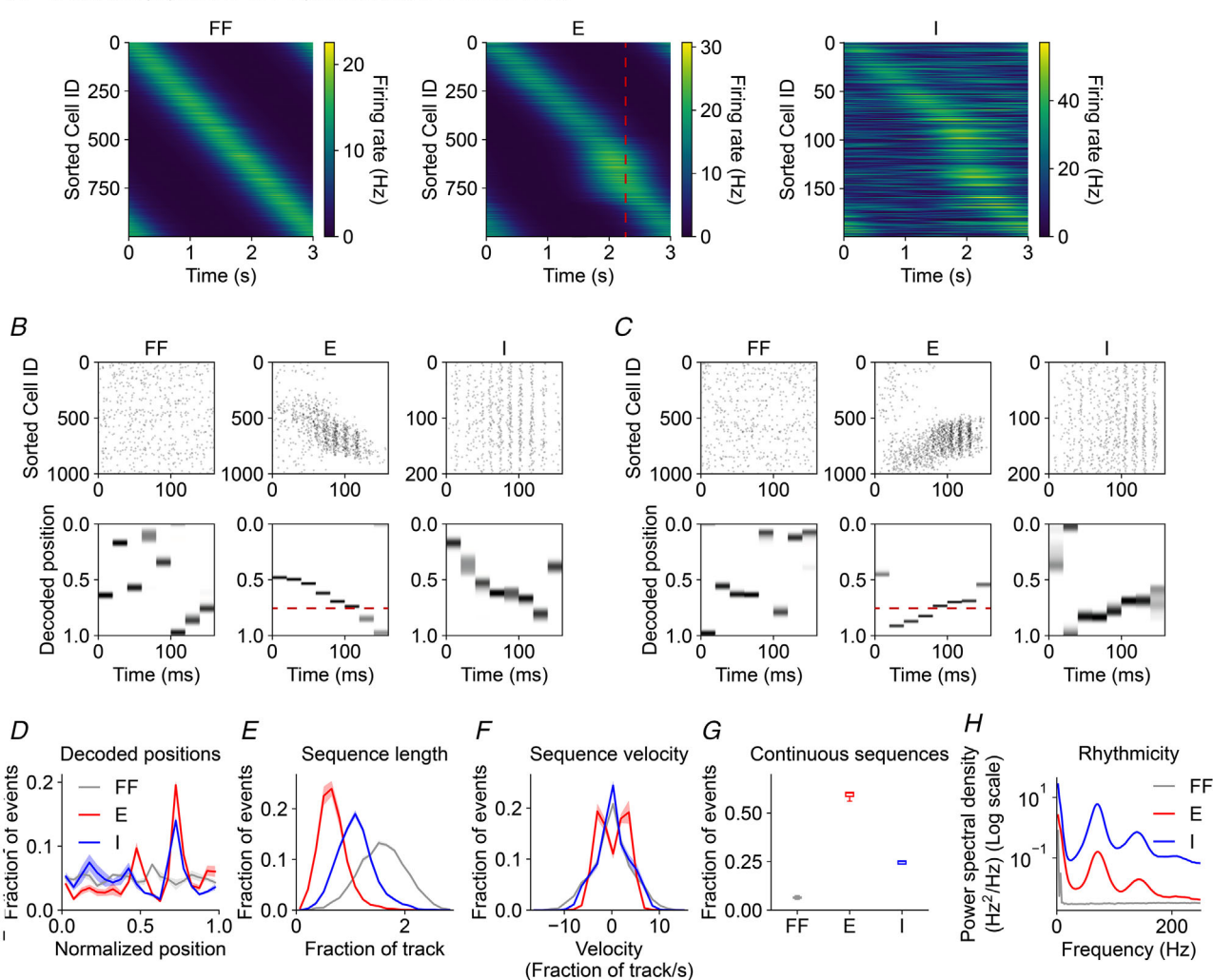


Figure 6. Offline memory replay is biased towards reward positions over-represented by the network A, in this variant of the network, an increased proportion of E cells are selective for spatial positions near the site of a simulated reward. Firing rates vs. time of all neurons in each cell population are shown (average of five trials from one example network instance). Cells in each population are sorted by the location of maximum firing. The simulated reward site is marked with red dashed line. B-H, same as Figs 3A-G for an alternative network model with population-level over-representation of reward location in E cells. B and C correspond to two example trials from one example network instance. The simulated reward site is marked with red dashed line. D, decoded positions (two-sided K-S tests: E vs. FF, P < 0.00001; I vs. FF, P = 0.41580; two-sided K-S tests vs. data from model with structured E  $\leftarrow$  E weights in Fig. 3C: E, P < 0.00001; I, P = 0.84875). E, offline sequence length (two-sided K-S tests: E vs. FF, P < 0.00001; I vs. FF, P < 0.00001; two-sided K-S tests vs. data from model with structured E  $\leftarrow$  E weights in Fig. 3D: E, P = 0.25150; I, P < 0.00001). F, offline sequence velocity (two-sided K-S tests: E vs. FF, P = 0.02742; I vs. FF, P = 0.73515; two-sided K-S tests vs. data from model with structured E  $\leftarrow$  E weights in Fig. 3E: E, P = 0.16847; I, P = 0.62023). G, fraction of events that met criterion for sequences consistent with continuous spatial trajectories (see Methods) (one-sided paired t tests: E vs. FF, P < 0.00001, I vs. FF, P = 0.00027; two-sided t tests vs. data from model with structured  $E \leftarrow E$  weights in Fig. 3F: E, P = 0.05397; I, P = 0.00754). H, offline high-frequency rhythmicity (one-sided paired t tests: 75–300 Hz frequency band: E vs. FF, P = 0.00067; I vs. FF, P = 0.00006; two-sided t tests vs. data from model with structured  $E \leftarrow E$  weights in Fig. 3G: E, P = 0.00003; I, P = 0.00001). In D-F and H, means (continuous line)  $\pm$  SEM (shading) were computed across five independent instances of each network. In G, box and whisker plots depict data from five independent instances of each network model (see Methods). P-values reflect FDR correction for multiple comparisons.

14697793, 2023, 15, Downloaded from https://phtysoc.onlinelibrary.wiley.com/doi/10.1113/JP283216, Wiley Online Library on [29/02/2024]. See the Terms and Conditions (https://onlinelibrary.wiley.com/terms-and-conditions) on Wiley Online Library for rules of use; OA articles are governed by the applicable Cerative Commons Licensean Conditions (https://onlinelibrary.wiley.com/terms-and-conditions) on Wiley Online Library for rules of use; OA articles are governed by the applicable Cerative Commons Licensean Conditions (https://onlinelibrary.wiley.com/terms-and-conditions) on Wiley Online Library for rules of use; OA articles are governed by the applicable Cerative Commons Licensean Conditions (https://onlinelibrary.wiley.com/terms-and-conditions) on Wiley Online Library for rules of use; OA articles are governed by the applicable Cerative Commons Licensean Conditions (https://onlinelibrary.wiley.com/terms-and-conditions) on Wiley Online Library for rules of use; OA articles are governed by the applicable Cerative Commons Licensean Conditions (https://onlinelibrary.wiley.com/terms-and-conditions) on Wiley Online Library for rules of use; OA articles are governed by the applicable Cerative Commons Licensean Conditions (https://onlinelibrary.wiley.com/terms-and-conditions) on Wiley Online Library for rules of use; OA articles are governed by the applicable Cerative Commons (https://onlinelibrary.wiley.com/terms-and-conditions) on the articles are governed by the applicable Cerative Commons (https://onlinelibrary.wiley.com/terms-and-conditions) on the articles are governed by the applicable Cerative Commons (https://onlinelibrary.wiley.com/terms-and-conditions) on the articles are governed by the applicable Cerative Commons (https://onlinelibrary.wiley.com/terms-and-conditions) on the articles are governed by the applicable Cerative Commons (https://onlinelibrary.wiley.com/terms-and-conditions) on the articles are governed by the ar

sequences of place cells that encode positions nearby and including the site of the reward (Gillespie et al., 2021; Ólafsdóttir et al., 2018; Pfeiffer, 2020; Singer & Frank, 2009). In parallel with the development of this bias in offline memory replay during learning, it has been shown that the fraction of hippocampal pyramidal cells that selectively fire along the path to reward increases (Lee et al., 2006; Turi et al., 2019; Zaremba et al., 2017). Here we sought to test the hypothesis that this network-level over-representation of reward location is sufficient to bias the content of offline memory replay.

We chose a position along the virtual track to be the fixed location of a simulated reward, and biased the allocation of place field locations such that an increased fraction of excitatory neurons were selectively activated at positions near the reward (Fig. 6A). As before, feedforward and recurrent synaptic connection strengths were increased between neurons with overlapping selectivity (Supplementary Fig. S9A). Aside from an enhanced fraction of active excitatory neurons near the reward site (Supplementary Fig. S9B), this produced network dynamics during simulated navigation that conformed to experimental constraints for sparsity, selectivity and rhythmicity (Fig. 6A and Supplementary Fig. S9B-E). During simulated offline rest, the excitatory neurons in the network responded to random feedforward inputs by generating neuronal sequences corresponding to forward, reverse and mixed direction trajectories through the environment (Fig. 6B-G), paced by high frequency oscillations in the inhibitory cells (Fig. 6H), as before (Fig. 3A–G). However, now positions near the simulated reward site were replayed in a higher proportion of replay events (Fig. 6D). This preferential replay of locations over-represented by the network recapitulated experimental findings and supported the hypothesis that non-uniform place cell allocation and biased memory replay are causally linked (Levy, 1989).

## **Discussion**

In this study we used a simple recurrent spiking network model of hippocampal area CA3 to investigate the structural and functional requirements for offline replay of spatial memories. We optimized synaptic, cellular and network parameters of the network to produce population dynamics that match experimentally observed sparsity, selectivity and rhythmicity. We found that networks that fit these constraints exhibit additional emergent properties, including the ability to generate fast timescale memory-related neuronal sequences. During simulated spatial navigation, when ordered sensory information was provided on the seconds-long timescale of locomotion behaviour, the network produced neuronal sequences that swept from past to future positions on the faster timescale

(~125 ms) of the theta rhythm ('theta sequences'). During simulated offline rest, the network responded to transient noisy activation of random, sparse inputs by generating neuronal sequences that corresponded to forward, reverse or mixed direction trajectories through the spatial environment.

Both online and offline sequence generation depended on structure in the strengths of excitatory synaptic connections such that pairs of neurons with overlapping spatial tuning were more strongly connected. In the online phase, different sparse subsets of excitatory neurons were activated at different spatial positions due to structure in the strengths of connections from spatially tuned feedforward afferent inputs. The constraint that recurrent excitation must drive rhythmic synchronization in the theta band resulted in relatively strong recurrent connections. During each cycle of the theta rhythm, when the firing rates of the excitatory neurons were at their maximum, synaptic excitation from recurrent connections exceeded that from the feedforward afferents (Supplementary Fig. S1E). This caused the sum of forward-moving feedforward inputs and symmetric mixed-direction feedback inputs to favour activation of cells encoding positions at or ahead of the current position. This generated forward-sweeping sequences that outpaced the speed of locomotion. However, at the opposite phase of the theta rhythm, when the firing rates of the excitatory cells reached their minimum, the non-rhythmic feedforward input became greater than recurrent excitation (Supplementary Fig. S1E), causing theta sequences to reverse direction and relax back towards the current position encoded by the feedforward

In the offline phase, the feedforward inputs were not activated in a sequence, so momentum had to be entirely internally generated by the network. In this case, the particular subset of active feedforward inputs initially selected a sparse subset of excitatory neurons to begin to fire, which set a starting position for the replayed trajectory. Slight biases in the feedforward input could then influence whether the active ensemble of excitatory neurons next recruited neurons encoding spatial positions in either the forward or reverse direction. Once activity began moving in one direction, spike-rate adaptation facilitated continued sequence movement along that direction. However, depending on fluctuations in the feedforward inputs, sequences were also generated that included changes in direction. Interestingly, this process is akin to interpolation or smoothing - the recurrent connections within the network served to bridge large, discontinuous jumps in position encoded by the noisy feedforward inputs with smaller, more continuous steps. This produced offline sequences that were consistent with the topology of the spatial environment, but did not necessarily replay exact experienced trajectories. These

findings are consistent with a recent report that neuronal sequences activated during hippocampal SWRs in vivo resembled Brownian motion, or a random walk through the sensory space, rather than precise replay of experience (Stella et al., 2019). This suggests that, rather than serving mainly to consolidate specific episodic memories of ordered sensory experiences, neuronal sequences during SWRs could also explore possible associations within the environment that had not been fully sampled during experience. Our modelling results showing that increased population representations of goal sites bias the content of offline memory replay also corroborate recent findings that previously rewarded locations are replayed more readily than immediate past or immediate future trajectories (Gillespie et al., 2021). Within this framework, synaptic plasticity during offline replay could modify connection strengths to increase the chance that a new path will be taken that is likely to lead to a desired outcome (Ólafsdóttir et al., 2015).

In summary, our modelling results identified a minimal set of elements sufficient to enable flexible and bidirectional memory replay in neuronal networks: spike rate adaptation, recurrent connectivity between excitatory and inhibitory neuron populations with strengths and kinetics optimized for rhythmogenesis and sparse and selective stimulus representations, and associative structure in the synaptic strengths at recurrent synapses between excitatory neurons. In previous models of neuronal sequence generation, additional network components were proposed to enable unidirectional sequences stored in memory to be reversed during offline recall, including neuromodulation (Gauy et al., 2018), excitability of neuronal dendrites (Gauy et al., 2018; Jahnke et al., 2015), coordinated plasticity at both excitatory and inhibitory synapses (Ramirez-Villegas et al., 2018) and functional specialization of diverse subpopulations of inhibitory interneurons (Cutsuridis & Hasselmo, 2011). While these mechanisms may regulate and enhance memory replay, our results suggest that they are not necessarily required.

This model also makes some experimentally testable predictions. First, it implies that ion channel mutations that disrupt neuronal spike rate adaptation may also degrade neuronal sequence generation and memory consolidation (Peters et al., 2005). Secondly, while the direction and content of offline sequences may be largely controlled by internal dynamics and information stored in the synaptic weights within a recurrent neuronal circuit, the model network still required a small amount of random feedforward afferent input to evoke an offline population burst, suggesting that experimental manipulations of afferent projections to hippocampal area CA3 may alter the frequency or content of memory replay events (Chenani et al., 2019; Sasaki et al., 2018).

Recent work has also begun to explore the advantages of generative replay for learning in artificial neural networks (Roscow et al., 2021). In addition to better understanding the biological mechanisms of memory consolidation and flexible planning of behaviour, characterizing the minimal mechanisms of memory replay could facilitate the engineering of artificial systems that can refine their internal representations of the environment during periods of offline rest (Buzsáki, 1989).

### References

- Amit, D. J., & Brunel, N. (1997). Dynamics of a recurrent network of spiking neurons before and following learning. *Network: Computation in Neural Systems*, **8**(4), 373–404.
- Arkhipov, A., Gouwens, N. W., Billeh, Y. N., Gratiy, S., Iyer, R., Wei, Z., Xu, Z., Abbasi-Asl, R., Berg, J., Buice, M., Cain, N., da Costa, N., de Vries, S., Denman, D., Durand, S., Feng, D., Jarsky, T., Lecoq, J., Lee, B., ... Koch, C. (2018). Visual physiology of the layer 4 cortical circuit in silico. *PLoS Computational Biology*, **14**(11), e1006535.
- Bezaire, M. J., Raikov, I., Burk, K., Vyas, D., & Soltesz, I.(2016). Interneuronal mechanisms of hippocampal theta oscillation in a full-scale model of the rodent CA1 circuit. *eLife*, 5, e18566.
- Bittner, K. C., Grienberger, C., Vaidya, S. P., Milstein, A. D., Macklin, J. J., Suh, J., Tonegawa, S., & Magee, J. C. (2015). Conjunctive input processing drives feature selectivity in hippocampal CA1 neurons. *Nature Neuroscience*, **18**(8), 1133–1142.

4697793, 2023, 15, Downloaded from https://physoc.onlinelibrary.wiley.com/doi/10.1113/P283216, Wiley. Online Library on [29/02/2024]. See the Terms and Conditions (https://onlinelibrary.wiley.com/terms-and-conditions) on Wiley Online Library for rules of use; OA articles are governed by the applicable Certain Commons License

- Bittner, K. C., Milstein, A. D., Grienberger, C., Romani, S., & Magee, J. C.(2017). Behavioral time scale synaptic plasticity underlies CA1 place fields. *Science*, **357**(6355), 1033–1036.
- Brunel, N.(2016). Is cortical connectivity optimized for storing information? *Nature Neuroscience*, **19**(5), 749–755.
- Brunel, N., & Trullier, O.(1998). Plasticity of directional place fields in a model of rodent CA3. *Hippocampus*, **8**(6), 651–665.
- Brunel, N., & Wang, X.-J.(2003). What determines the frequency of fast network oscillations with irregular neural discharges? I. Synaptic dynamics and excitation-inhibition balance. *Journal of Neurophysiology*, **90**(1), 415–430.
- Buzsáki, G.(1989). Two-stage model of memory trace formation: A role for "noisy" brain states. *Neuroscience*, **31**(3), 551–570.
- Buzsáki, G., McKenzie, S., & Davachi, L.(2021). Neurophysiology of remembering. *Annual Review of Psychology*, 73(1), 187–215.
- Buzsaki, G., & Mizuseki, K.(2014). The log-dynamic brain: How skewed distributions affect network operations. *Nature Reviews Neuroscience*, **15**(4), 264–278.
- Carnevale, N. T., & Hines, M. L.(2006). *The NEURON book*. Cambridge University Press.
- Chadwick, A., van Rossum, M. C., & Nolan, M. F.(2015). Independent theta phase coding accounts for CA1 population sequences and enables flexible remapping. *eLife*, **4**, e03542.

- Chadwick, A., van Rossum, M. C., & Nolan, M. F.(2016). Flexible theta sequence compression mediated via phase precessing interneurons. *eLife*, **5**, e20349.
- Chenani, A., Sabariego, M., Schlesiger, M. I., Leutgeb, J. K., Leutgeb, S., & Leibold, C.(2019). Hippocampal CA1 replay becomes less prominent but more rigid without inputs from medial entorhinal cortex. *Nature Communications*, **10**(1), 1341.
- Colgin, L. L.(2016). Rhythms of the hippocampal network. *Nature Reviews. Neuroscience*, **17**(4), 239–249.
- Csicsvari, J., Hirase, H., Mamiya, A., & Buzsaki, G.(2000). Ensemble patterns of hippocampal CA3-CA1 neurons during sharp wave-associated population events. *Neuron*, **28**(2), 585–594.
- Csicsvari, J., Jamieson, B., Wise, K. D., & Buzsaki, G.(2003). Mechanisms of gamma oscillations in the hippocampus of the behaving rat. *Neuron*, 37(2), 311–322.
- Cutsuridis, V., & Hasselmo, M.(2011). Spatial memory sequence encoding and replay during modeled theta and ripple oscillations. *Cognitive Computation*, **3**(4), 554–574.
- Davidson, T. J., Kloosterman, F., & Wilson, M. A.(2009). Hippocampal replay of extended experience. *Neuron*, **63**(4), 497–507.
- de Almeida, L., Idiart, M., & Lisman, J. E.(2007). Memory retrieval time and memory capacity of the CA3 network: role of gamma frequency oscillations. *Learning & Memory*, **14**(11), 795–806.
- de Almeida, L., Idiart, M., & Lisman, J. E.(2009a). A second function of gamma frequency oscillations: An E%-max winner-take-all mechanism selects which cells fire. *Journal of Neuroscience*, **29**(23), 7497–7503.
- de Almeida, L., Idiart, M., & Lisman, J. E.(2009b). The input-output transformation of the hippocampal granule cells: From grid cells to place fields. *Journal of Neuroscience*, **29**(23), 7504–7512.
- Deb, K.(2011). Multi-objective evolutionary optimisation for product design and manufacturing. 3–34.
- Dorkenwald, S., Turner, N. L., Macrina, T., Lee, K., Lu, R., Wu, J., Bodor, A. L., Bleckert, A. A., Brittain, D., Kemnitz, N., Silversmith, W. M., Ih, D., Zung, J., Zlateski, A., Tartavull, I., Yu, S.-C., Popovych, S., Wong, W., Castro, M., ... Seung, H. S. (2019). Binary and analog variation of synapses between cortical pyramidal neurons. Biorxiv 2019.12.29.890319.
- Dragoi, G., & Tonegawa, S.(2013). Distinct preplay of multiple novel spatial experiences in the rat. *Proceedings of the National Academy of Sciences, USA*, **110**(22), 9100–9105.
- Drieu, C., & Zugaro, M.(2019). Hippocampal sequences during exploration: Mechanisms and functions. *Frontiers in Cellular Neuroscience*, **13**, 232.
- Duigou, C. L., Simonnet, J., Teleñczuk, M. T., Fricker, D., & Miles, R.(2014). Recurrent synapses and circuits in the CA3 region of the hippocampus: An associative network. *Frontiers in Cellular Neuroscience*, 7, 262.
- Ecker, A., Bagi, B., Vértes, E., Steinbach-Németh, O., Karlócai, M. R., Papp, O. I., Miklós, I., Hájos, N., Freund, T. F., Gulyás, A. I., & Káli, S.(2022). Hippocampal sharp wave-ripples and the associated sequence replay emerge from structured synaptic interactions in a network model of area CA3. *eLife*, 11, e71850.

- Ego-Stengel, V., & Wilson, M. A.(2007). Spatial selectivity and theta phase precession in CA1 interneurons. *Hippocampus*, **17**(2), 161–174.
- Ermentrout, B.(1992). Complex dynamics in winner-take-all neural nets with slow inhibition. *Neural Networks*, **5**(3), 415–431.
- Farooq, U., & Dragoi, G.(2019). Emergence of preconfigured and plastic time-compressed sequences in early postnatal development. *Science*, 363(6423), 168–173.
- Fernández-Ruiz, A., Oliva, A., de Oliveira, E. F., Rocha-Almeida, F., Tingley, D., & Buzsáki, G.(2019). Long-duration hippocampal sharp wave ripples improve memory. *Science*, **364**(6445), 1082–1086.
- Foster, D. J., & Wilson, M. A.(2007). Hippocampal theta sequences. *Hippocampus*, **17**(11), 1093–1099.
- Gauy, M. M., Lengler, J., Einarsson, H., Meier, F., Weissenberger, F., Yanik, M. F., & Steger, A.(2018). A hippocampal model for behavioral time acquisition and fast bidirectional replay of spatio-temporal memory sequences. *Frontiers in Neuroscience*, **12**, 961.
- Geiller, T., Vancura, B., Terada, S., Troullinou, E., Chavlis, S.,
  Tsagkatakis, G., Tsakalides, P., Ócsai, K., Poirazi, P., Rózsa,
  B. J., & Losonczy, A.(2020). Large-scale 3D two-photon imaging of molecularly identified CA1 interneuron dynamics in behaving mice. *Neuron*, 108(5), 968–983.e9.
- Geisler, C., Brunel, N., & Wang, X.-J.(2005). Contributions of intrinsic membrane dynamics to fast network oscillations with irregular neuronal discharges. *Journal of Neuro-physiology*, **94**(6), 4344–4361.
- Gillespie, A. K., Maya, D. A. A., Denovellis, E. L., Liu, D. F., Kastner, D. B., Coulter, M. E., Roumis, D. K., Eden, U. T., & Frank, L. M.(2021). Hippocampal replay reflects specific past experiences rather than a plan for subsequent choice. *Neuron*, 109(19), 3149–3163.e6.
- Girardeau, G., Benchenane, K., Wiener, S. I., Buzsáki, G., & Zugaro, M. B. (2009). Selective suppression of hippocampal ripples impairs spatial memory. *Nature Neuroscience*, **12**(10), 1222–1223.
- Grienberger, C., Milstein, A. D., Bittner, K. C., Romani, S., & Magee, J. C.(2017). Inhibitory suppression of heterogeneously tuned excitation enhances spatial coding in CA1 place cells. *Nature Neuroscience*, **20**(3), 417–426.
- Griniasty, M., Tsodyks, M. V., & Amit, D. J. (1993). Conversion of temporal correlations between stimuli to spatial correlations between attractors. *Neural Computation*, 5(1), 1–17.
- Grosmark, A. D., & Buzsáki, G. (2016). Diversity in neural firing dynamics supports both rigid and learned hippocampal sequences. *Science*, **351**(6280), 1440–1443.
- Gupta, A. S., van der Meer, M. A. A., Touretzky, D. S., & Redish, A. D. (2010). Hippocampal replay is not a simple function of experience. *Neuron*, **65**(5), 695–705.
- Guzman, S. J., Schlogl, A., Frotscher, M., & Jonas, P.(2016). Synaptic mechanisms of pattern completion in the hippocampal CA3 network. *Science*, **353**(6304), 1117–1123.
- Hangya, B., Li, Y., Muller, R. U., & Czurkó, A. (2010). Complementary spatial firing in place cell-interneuron pairs. *The Journal of Physiology*, **588**(21), 4165–4175.
- Hines, M. L., Davison, A. P., & Muller, E. (2009). NEURON and Python. Frontiers in Neuroinformatics, 3, 1.

- Hopfield, J. J. (1982). Neural networks and physical systems with emergent collective computational abilities. *Proceedings of the National Academy of Sciences, USA*, **79**(8), 2554–2558.
- Igata, H., Ikegaya, Y., & Sasaki, T. (2021). Prioritized experience replays on a hippocampal predictive map for learning. *Proceedings of the National Academy of Sciences, USA*, **118**(1), e2011266118.
- Itskov, V., Curto, C., Pastalkova, E., & Buzsáki, G.(2011). Cell assembly sequences arising from spike threshold adaptation keep track of time in the hippocampus. *Journal of Neuroscience*, **31**(8), 2828–2834.
- Izhikevich, E. M. (2007). *Dynamical systems in neuroscience*. MIT Press.
- Izhikevich, E. M., & Edelman, G. M. (2008). Large-scale model of mammalian thalamocortical systems. *Proceedings of the National Academy of Sciences, USA*, **105**(9), 3593–3598.
- Jadhav, S. P., Kemere, C., German, P. W., & Frank, L. M. (2012). Awake hippocampal sharp-wave ripples support spatial memory. *Science*, 336(6087), 1454–1458.
- Jahnke, S., Timme, M., & Memmesheimer, R. M.(2015). A unified dynamic model for learning, replay, and sharp-wave/ripples. *Journal of Neuroscience*, 35(49), 16236–16258.
- Jensen, O., Idiart, M. A., & Lisman, J. E. (1996). Physiologically realistic formation of autoassociative memory in networks with theta/gamma oscillations: Role of fast NMDA channels. *Learning & Memory*, **3**(2–3), 243–256.
- Joo, H. R., & Frank, L. M. (2018). The hippocampal sharp wave-ripple in memory retrieval for immediate use and consolidation. *Nature Reviews. Neuroscience*, 19(12), 744–757.
- Káli, S., & Dayan, P.(2000). The involvement of recurrent connections in area CA3 in establishing the properties of place fields: A model. *Journal of Neuroscience*, **20**(19), 7463–7477.
- Kang, L., & DeWeese, M. R.(2019). Replay as wavefronts and theta sequences as bump oscillations in a grid cell attractor network. *eLife*, **8**, e46351.
- Kay, K., Chung, J. E., Sosa, M., Schor, J. S., Karlsson, M. P., Larkin, M. C., Liu, D. F., & Frank, L. M.(2020). Constant sub-second cycling between representations of possible futures in the hippocampus. *Cell*, **180**(3), 552–567.e25.
- Lee, I., Griffin, A. L., Zilli, E. A., Eichenbaum, H., & Hasselmo, M. E.(2006). Gradual translocation of spatial correlates of neuronal firing in the hippocampus toward prospective reward locations. *Neuron*, 51(5), 639–650.
- Levy, W. B. (1989). A computational approach to hippocampal function. *Psychology of Learning and Motivation*, 23, 243–305.
- Lisman, J. E., & Jensen, O. (2013). The theta-gamma neural code. *Neuron*, 77(6), 1002–1016.
- Lisman, J. E., Talamini, L. M., & Raffone, A. (2005). Recall of memory sequences by interaction of the dentate and CA3:
  A revised model of the phase precession. *Neural Networks*, 18(9), 1191–1201.
- Luczak, A., Barthó, P., Marguet, S. L., Buzsáki, G., & Harris, K. D.(2007). Sequential structure of neocortical spontaneous activity in vivo. *Proceedings of the National Academy of Sciences*, USA, 104(1), 347–352.

- Lytton, W. W., Seidenstein, A. H., Dura-Bernal, S., McDougal, R. A., Schürmann, F., & Hines, M. L. (2016). Simulation neurotechnologies for advancing brain research: Parallelizing large networks in NEURON. *Neural Computation*, **28**(10), 2063–2090.
- Malerba, P., & Bazhenov, M. (2019). Circuit mechanisms of hippocampal reactivation during sleep. *Neurobiology of Learning and Memory*, **160**, 98–107.
- Marder, E., & Taylor, A. L. (2011). Multiple models to capture the variability in biological neurons and networks. *Nature Neuroscience*, 14(2), 133–138.
- Marr, D.(1971). Simple memory: A theory for archicortex. *Philosophical Transactions of the Royal Society of London B Biological Sciences*, **262**(841), 23–81.
- Marshall, L., Henze, D. A., Hirase, H., Leinekugel, X., Dragoi, G., & Buzsáki, G. (2002). Hippocampal pyramidal cell–interneuron spike transmission is frequency dependent and responsible for place modulation of interneuron discharge. *Journal of Neuroscience*, **22**(2), RC197–RC197.
- McNaughton, B. L., & Morris, R. G. M.(1987). Hippocampal synaptic enhancement and information storage within a distributed memory system. *Trends in Neurosciences*, **10**(10), 408–415.
- Mehta, M. R., Lee, A. K., & Wilson, M. A. (2002). Role of experience and oscillations in transforming a rate code into a temporal code. *Nature*, **417**(6890), 741–746.
- Milstein, A. D., Li, Y., Bittner, K. C., Grienberger, C., Soltesz, I., Magee, J. C., & Romani, S. (2021). Bidirectional synaptic plasticity rapidly modifies hippocampal representations. *eLife*, **10**, e73046.

14697793, 2023, 15, Downloaded from https://phtysoc.onlinelibrary.wiley.com/doi/10.1113/JP283216, Wiley Online Library on [29/02/2024]. See the Terms and Conditions (https://onlinelibrary.wiley.com/terms-and-conditions) on Wiley Online Library for rules of use; OA articles are governed by the applicable Cerative Commons Licensean Conditions (https://onlinelibrary.wiley.com/terms-and-conditions) on Wiley Online Library for rules of use; OA articles are governed by the applicable Cerative Commons Licensean Conditions (https://onlinelibrary.wiley.com/terms-and-conditions) on Wiley Online Library for rules of use; OA articles are governed by the applicable Cerative Commons Licensean Conditions (https://onlinelibrary.wiley.com/terms-and-conditions) on Wiley Online Library for rules of use; OA articles are governed by the applicable Cerative Commons Licensean Conditions (https://onlinelibrary.wiley.com/terms-and-conditions) on Wiley Online Library for rules of use; OA articles are governed by the applicable Cerative Commons Licensean Conditions (https://onlinelibrary.wiley.com/terms-and-conditions) on Wiley Online Library for rules of use; OA articles are governed by the applicable Cerative Commons Licensean Conditions (https://onlinelibrary.wiley.com/terms-and-conditions) on Wiley Online Library for rules of use; OA articles are governed by the applicable Cerative Commons (https://onlinelibrary.wiley.com/terms-and-conditions) on the articles are governed by the applicable Cerative Commons (https://onlinelibrary.wiley.com/terms-and-conditions) on the articles are governed by the applicable Cerative Commons (https://onlinelibrary.wiley.com/terms-and-conditions) on the articles are governed by the applicable Cerative Commons (https://onlinelibrary.wiley.com/terms-and-conditions) on the articles are governed by the applicable Cerative Commons (https://onlinelibrary.wiley.com/terms-and-conditions) on the articles are governed by the ar

- Okamoto, K., & Ikegaya, Y. (2019). Recurrent connections between CA2 pyramidal cells. *Hippocampus*, **29**(4), 305–312.
- O'Keefe, J., & Conway, D. H. (1978). Hippocampal place units in the freely moving rat: Why they fire where they fire. *Experimental Brain Research*, **31**(4), 573–590.
- O'Keefe, J., & Recce, M. L.(1993). Phase relationship between hippocampal place units and the EEG theta rhythm. *Hippocampus*, **3**(3), 317–330.
- Ólafsdóttir, H. F., Barry, C., Saleem, A. B., Hassabis, D., & Spiers, H. J.(2015). Hippocampal place cells construct reward related sequences through unexplored space. *eLife*, **4**, e06063.
- Ólafsdóttir, H. F., Bush, D., & Barry, C.(2018). The role of hippocampal replay in memory and planning. *Current Biology*, **28**(1), R37–R50.
- Oliva, A., Fernandez-Ruiz, A., Buzsaki, G., & Berenyi, A.(2016). Role of hippocampal CA2 region in triggering sharp-wave ripples. *Neuron*, **91**(6), 1342–1355.
- O'Neill, J., Senior, T. J., Allen, K., Huxter, J. R., & Csicsvari, J. (2008). Reactivation of experience-dependent cell assembly patterns in the hippocampus. *Nature Neuroscience*, **11**(2), 209–215.
- Pelkey, K. A., Chittajallu, R., Craig, M. T., Tricoire, L., Wester, J. C., & McBain, C. J. (2017). Hippocampal GABAergic inhibitory interneurons. *Physiological Reviews*, **97**(4), 1619–1747.
- Peters, H. C., Hu, H., Pongs, O., Storm, J. F., & Isbrandt, D.(2005). Conditional transgenic suppression of M channels in mouse brain reveals functions in neuronal excitability, resonance and behavior. *Nature Neuroscience*, **8**(1), 51–60.

- Pfeiffer, B. E. (2020). The content of hippocampal "replay." *Hippocampus*, **30**(1), 6–18.
- Pfeiffer, B. E., & Foster, D. J. (2015). Autoassociative dynamics in the generation of sequences of hippocampal place cells. *Science*, **349**(6244), 180–183.
- Ramirez-Villegas, J. F., Willeke, K. F., Logothetis, N. K., & Besserve, M. (2018). Dissecting the synapse- and frequency-dependent network mechanisms of in vivo hippocampal sharp wave-ripples. *Neuron*, **100**(5), 1224–1240.e13.
- Reifenstein, E. T., Khalid, I. B., & Kempter, R.(2021). Synaptic learning rules for sequence learning. *eLife*, **10**, e67171.
- Renno-Costa, C., Lisman, J. E., & Verschure, P. F. (2014). A signature of attractor dynamics in the CA3 region of the hippocampus. *PLoS Computational Biology*, **10**(5), e1003641.
- Rennó-Costa, C., Teixeira, D. G., & Soltesz, I.(2019). Regulation of gamma-frequency oscillation by feedforward inhibition: A computational modeling study. *Hippocampus*, **29**(10), 957–970.
- Romani, S., & Tsodyks, M.(2015). Short-term plasticity based network model of place cells dynamics. *Hippocampus*, **25**(1), 94–105.
- Roscow, E. L., Chua, R., Costa, R. P., Jones, M. W., & Lepora, N. (2021). Learning offline: Memory replay in biological and artificial reinforcement learning. *Trends in Neurosciences*, 44(10), 808–821.
- Sasaki, T., Piatti, V. C., Hwaun, E., Ahmadi, S., Lisman, J. E., Leutgeb, S., & Leutgeb, J. K. (2018). Dentate network activity is necessary for spatial working memory by supporting CA3 sharp-wave ripple generation and prospective firing of CA3 neurons. *Nature Neuroscience*, **21**(2), 258–269.
- Scharfman, H. E. (1993). Spiny neurons of area CA3c in rat hippocampal slices have similar electrophysiological characteristics and synaptic responses despite morphological variation. *Hippocampus*, 3(1), 9–28.
- Singer, A. C., & Frank, L. M. (2009). Rewarded outcomes enhance reactivation of experience in the hippocampus. *Neuron*, **64**(6), 910–921.
- Skaggs, W. E., McNaughton, B. L., Wilson, M. A., & Barnes, C. A. (1996). Theta phase precession in hippocampal neuronal populations and the compression of temporal sequences. *Hippocampus*, **6**(2), 149–172.
- Soltesz, I., & Deschenes, M.(1993). Low- and high-frequency membrane potential oscillations during theta activity in CA1 and CA3 pyramidal neurons of the rat hippocampus under ketamine-xylazine anesthesia. *Journal of Neuro-physiology*, **70**(1), 97–116.
- Sompolinsky, H., & Kanter, I. (1986). Temporal association in asymmetric neural networks. *Physical Review Letter*, 57(22), 2861–2864.
- Stark, E., Roux, L., Eichler, R., & Buzsaki, G. (2015). Local generation of multineuronal spike sequences in the hippocampal CA1 region. *Proceedings of the National Academy of Sciences, USA*, **112**(33), 10521–10526.
- Stark, E., Roux, L., Eichler, R., Senzai, Y., Royer, S., & Buzsaki, G. (2014). Pyramidal cell-interneuron interactions underlie hippocampal ripple oscillations. *Neuron*, 83(2), 467–480.

- Stefanelli, T., Bertollini, C., Luscher, C., Muller, D., & Mendez, P. (2016). Hippocampal somatostatin interneurons control the size of neuronal memory ensembles. *Neuron*, 89(5), 1074–1085.
- Stella, F., Baracskay, P., O'Neill, J., & Csicsvari, J.(2019). Hippocampal reactivation of random trajectories resembling brownian diffusion. *Neuron*, **102**(2), 450–461.e7.
- Tremblay, R., Lee, S., & Rudy, B.(2016). GABAergic interneurons in the neocortex: From cellular properties to circuits. *Neuron*, **91**(2), 260–292.
- Treves, A.(2004). Computational constraints between retrieving the past and predicting the future, and the CA3-CA1 differentiation. *Hippocampus*, **14**(5), 539–556.
- Treves, A., & Rolls, E. T. (1994). Computational analysis of the role of the hippocampus in memory. *Hippocampus*, **4**(3), 374–391.
- Tsodyks, M. V., Skaggs, W. E., Sejnowski, T. J., & McNaughton, B. L. (1996). Population dynamics and theta rhythm phase precession of hippocampal place cell firing: A spiking neuron model. *Hippocampus*, **6**(3), 271–280.
- Tukker, J. J., Lasztoczi, B., Katona, L., Roberts, J. D., Pissadaki, E. K., Dalezios, Y., Marton, L., Zhang, L., Klausberger, T., & Somogyi, P. (2013). Distinct dendritic arborization and in vivo firing patterns of parvalbumin-expressing basket cells in the hippocampal area CA3. *Journal of Neuroscience*, 33(16), 6809–6825.
- Turi, G. F., Li, W.-K., Chavlis, S., Pandi, I., O'Hare, J., Priestley, J. B., Grosmark, A. D., Liao, Z., Ladow, M., Zhang, J. F.,
  B. V. Zemelman, P. Poirazi, & A. Losonczy (2019). Vasoactive intestinal polypeptide-expressing interneurons in the hippocampus support goal-oriented spatial learning. *Neuron*, 101(6), 1150–1165.e8.
- Wang, X.-J.(2010). Neurophysiological and computational principles of cortical rhythms in cognition. *Physiological Reviews*, **90**(3), 1195–1268.
- Wilent, W. B., & Nitz, D. A. (2007). Discrete place fields of hippocampal formation interneurons. *Journal of Neuro-physiology*, **97**(6), 4152–4161.
- Wu, X., & Foster, D. J. (2014). Hippocampal replay captures the unique topological structure of a novel environment. *Journal of Neuroscience*, **34**(19), 6459–6469.
- Ylinen, A., Soltesz, I., Bragin, A., Penttonen, M., Sik, A., & Buzsaki, G. (1995). Intracellular correlates of hippocampal theta rhythm in identified pyramidal cells, granule cells, and basket cells. *Hippocampus*, **5**(1), 78–90.
- Zaremba, J. D., Diamantopoulou, A., Danielson, N. B., Grosmark, A. D., Kaifosh, P. W., Bowler, J. C., Liao, Z., Sparks, F. T., Gogos, J. A., & Losonczy, A. (2017). Impaired hippocampal place cell dynamics in a mouse model of the 22q11.2 deletion. *Nature Neuroscience*, **20**(11), 1612–1623.
- Zhang, K., Ginzburg, I., McNaughton, B. L., & Sejnowski, T. J. (1998). Interpreting neuronal population activity by reconstruction: Unified framework with application to hippocampal place cells. *Journal of Neurophysiology*, **79**(2), 1017–1044.

#### **Additional information**

# Data availability statement

All code necessary to reproduce the data and analysis presented in this work are available here: Network simulation and analysis code: https://github.com/neurosutras/optimize\_simple\_network. Network optimization code: https://github.com/neurosutras/nested.

# **Competing interests**

None.

#### **Author contributions**

Conception or design of the work: A.M. and I.S. Acquisition or analysis or interpretation of data for the work: A.M., S.T. and G.N. Drafting the work or revising it critically for important intellectual content: A.M., S.T., G.N. and I.S. All authors have read and approved the final version of this manuscript and agree to be accountable for all aspects of the work in ensuring that questions related to the accuracy or integrity of any part of the work are appropriately investigated and resolved. All persons designated as authors qualify for authorship, and all those who qualify for authorship are listed.

#### **Funding**

This work was funded by National Institute of Mental Health (NIMH): A.M., R01MH121979; National Institute of Neurological Disorders and Stroke (NINDS): A.M., I.S., NS104590. This work was also made possible by computing allotments from NSF (XSEDE Comet, NCSA Blue Waters, and TACC Frontera).

# **Acknowledgements**

We are grateful to Kristopher Bouchard at LBNL for sharing large-scale computing resources provided by the National Energy Research Scientific Computing Center, a Department of Energy Office of Science User Facility (DE-AC02-05CH11231).

# **Keywords**

computational neuroscience, hippocampus, inhibition, mathematical model, memory, neural network, neuronal activity, oscillation

# **Supporting information**

Additional supporting information can be found online in the Supporting Information section at the end of the HTML view of the article. Supporting information files available:

**Figure S1**. Related to Figs 1–3. Structure and online dynamics of network model with excitatory synaptic connectivity structured by shared stimulus selectivity.

**Figure S2**. Related to Figs 1–3. Structure and online dynamics of alternative network models with random recurrent excitatory connectivity.

**Figure S3**. Related to Figs 1 and 3. Offline replay is unidirectional in an alternative network model with asymmetric synaptic connectivity.

**Figure S4**. Related to Fig. 3. Offline replay is disrupted in an alternative network model with structured, but shuffled recurrent excitatory connectivity.

**Figure S5**. Related to Figs 1 and 3. Offline replay is disrupted in an alternative network model optimized to suppress rhythmicity. **Figure S6**. Related to Figs 1 and 3. Offline replay is disrupted in an alternative network model optimized without sparsity or selectivity constraints.

**Figure S7**. Related to Figs 1 and 5. Online dynamics in network model without spike rate adaptation.

4697793, 2023, 15, Downloaded from https://physoc.onlinelibrary.wiley.com/doi/10.1113/P283216, Wiley. Online Library on [29/02/2024]. See the Terms and Conditions (https://onlinelibrary.wiley.com/terms-and-conditions) on Wiley Online Library for rules of use; OA articles are governed by the applicable Certain Commons License

**Figure S8**. Related to Figs 1, 3, 4, and 5. Exploration of model parameter diversity and degeneracy in additional alternative network models.

**Figure S9.** Related to Figs 1 and 6. Online activity in network model with population over-representation of reward.

Statistical Summary Document Peer Review History